

# Revisiting the ultraluminous supersoft source in M 101: an optically thick outflow model

Roberto Soria<sup>1\*</sup>, Albert K. H. Kong<sup>2</sup>

<sup>1</sup>*International Centre for Radio Astronomy Research, Curtin University, GPO Box U1987, Perth, WA 6845, Australia*

<sup>2</sup>*Institute of Astronomy and Department of Physics, National Tsing Hua University, Hsinchu 30013, Taiwan*

Accepted 2015 November 11

## ABSTRACT

The M 101 galaxy contains the best-known example of an ultraluminous supersoft source (ULS), dominated by a thermal component at  $kT \approx 0.1$  keV. The origin of the thermal component and the relation between ULSs and standard (broad-band spectrum) ultraluminous X-ray sources (ULXs) are still controversial. We re-examined the X-ray spectral and timing properties of the M 101 ULS using archival *Chandra* and *XMM-Newton* observations. We show that the X-ray time-variability and spectral properties are inconsistent with standard disk emission. The characteristic radius  $R_{\text{bb}}$  of the thermal emitter varies from epoch to epoch between  $\approx 10,000$  km and  $\approx 100,000$  km; the colour temperature  $kT_{\text{bb}}$  varies between  $\approx 50$  eV and  $\approx 140$  eV; and the two quantities scale approximately as  $R_{\text{bb}} \propto T_{\text{bb}}^{-2}$ . In addition to the smooth continuum, we also find (at some epochs) spectral residuals well fitted with thermal plasma models and absorption edges: we interpret this as evidence that we are looking at a clumpy, multi-temperature outflow. We suggest that at sufficiently high accretion rates and inclination angles, the super-critical, radiatively driven outflow becomes effectively optically thick and completely thermalizes the harder X-ray photons from the inner part of the inflow, removing the hard spectral tail. We develop a simple, spherically symmetric outflow model and show that it is consistent with the observed temperatures, radii and luminosities. A larger, cooler photosphere shifts the emission peak into the far-UV and makes the source dimmer in X-rays but possibly ultraluminous in the UV. We compare our results and interpretation with those of Liu et al. (2013).

**Key words:** accretion, accretion discs – X-rays: individual: M 101 ULX-1 – black hole physics.

## 1 INTRODUCTION

Ultraluminous X-ray sources (ULXs) are the highest-luminosity group of the X-ray binary population, empirically defined by an X-ray luminosity  $L_{\text{X}} \gtrsim 3 \times 10^{39}$  erg s<sup>-1</sup> (Feng & Soria 2011 for a review). In most cases, the simplest explanation consistent with the observations is that ULXs contain a stellar-mass black hole (BH) accreting above its Eddington limit (Gladstone et al. 2009; Sutton et al. 2013; Motch et al. 2014). In our Galaxy, the masses of stellar BHs are clustered around  $\approx 5\text{--}15M_{\odot}$  (Kreidberg et al. 2012); however, in lower-metallicity galaxies, stellar evolution models allow for the formation of BHs as massive as  $\approx 80M_{\odot}$  (Belczynski et al. 2010), corresponding to an Eddington luminosity  $\approx 10^{40}$  erg s<sup>-1</sup>. When the accretion rate is super-critical ( $\dot{m} \equiv 0.1Mc^2/L_{\text{Edd}} > 1$ ), the photon luminosity

mildly exceeds the Eddington limit:  $L \approx L_{\text{Edd}}(1 + a \ln \dot{m})$  where  $3/5 \lesssim a \lesssim 1$  depending on the relative fraction of energy carried by outflows or advected through the BH horizon (Poutanen et al. 2007; Shakura & Sunyaev 1973).

The X-ray spectral appearance of ULXs depends both on accretion rate and, for a given  $\dot{m}$ , on the viewing angle (Sutton et al. 2013). Sources that only mildly exceed the critical rate ( $\dot{m} \lesssim$  a few) have a curved, thermal spectrum consistent with a non-standard accretion disk (slim disk models: Watarai et al. 2001; Mizuno et al. 2001; Kubota & Makishima 2004), with characteristic inner-disk temperatures  $kT_{\text{in}} \approx 1.3\text{--}2$  keV and a flatter radial temperature profile. At higher accretion rates, the X-ray spectra of most ULXs show a slightly curved broad-band component dominating the 1–10 keV band, with an additional thermal component (soft excess) at  $kT_{\text{bb}} \approx 0.15\text{--}0.30$  keV. The origin of both components is still disputed. The broader component could come either from the inner part of the non-standard accretion disk, or from inverse-Compton scattering

\* E-mail: roberto.soria@icrar.org (RS); akong@phys.nthu.edu.tw (AKHK)

Date	ObsID	Exposure time (ks)	0.3–2 keV Net Count Rate ( $10^{-4}$ ct s $^{-1}$ )	$L_{0.3-10}^{\min}$ (erg s $^{-1}$ )
2000 Mar 26	934	98.38	$914 \pm 10$	$(1.6_{-0.1}^{+0.1}) \times 10^{39}$
2000 Oct 29	2065	9.63	$297 \pm 18$	$(6.3_{-0.9}^{+0.5}) \times 10^{38}$
2004 Jan 19	4731	56.24	$3.0 \pm 0.8$	$(1.7_{-0.5}^{+0.5}) \times 10^{37}$
2004 Jan 24	5297	21.69	$4.7 \pm 1.5$	$(2.7_{-0.8}^{+0.8}) \times 10^{37}$
2004 Mar 07	5300	52.09	$4.3 \pm 1.0$	$(2.5_{-0.6}^{+0.6}) \times 10^{37}$
2004 Mar 14	5309	70.77	$2.3 \pm 0.6$	$(1.3_{-0.3}^{+0.3}) \times 10^{37}$
2004 Mar 19	4732	69.79	$2.0 \pm 0.6$	$(1.2_{-0.4}^{+0.4}) \times 10^{37}$
2004 May 03	5322	64.7	$1.8 \pm 0.6$	$(1.0_{-0.3}^{+0.3}) \times 10^{37}$
2004 May 07	4733	24.81	$2.2 \pm 1.1$	$(1.3_{-0.7}^{+0.7}) \times 10^{37}$
2004 May 09	5323	42.62	$1.9 \pm 0.7$	$(1.1_{-0.4}^{+0.4}) \times 10^{37}$
2004 Jul 05	5337	9.94	$196 \pm 14$	$(9.0_{-1.0}^{+1.0}) \times 10^{38}$
2004 Jul 06	5338	28.57	$260 \pm 10$	$(9.4_{-1.0}^{+0.8}) \times 10^{38}$
2004 Jul 07	5339	14.32	$231 \pm 13$	$(8.4_{-1.0}^{+1.0}) \times 10^{38}$
2004 Jul 08	5340	54.42	$102 \pm 4$	$(4.5_{-0.6}^{+1.0}) \times 10^{38}$
2004 Jul 11	4734	35.48	$67 \pm 4$	$(4.0_{-0.6}^{+0.6}) \times 10^{38}$
2004 Jul 23	0164560701	21.1	$58 \pm 8$	$(6.8_{-1.3}^{+1.3}) \times 10^{37}$
2004 Sep 05	6114	66.2	$3.0 \pm 0.7$	$(1.7_{-0.4}^{+0.4}) \times 10^{37}$
2004 Sep 08	6115	35.76	$2.5 \pm 0.9$	$(1.4_{-0.6}^{+0.6}) \times 10^{37}$
2004 Sep 11	6118	11.46	$3.9 \pm 2.0$	$(2.3_{-1.2}^{+1.2}) \times 10^{37}$
2004 Sep 12	4735	28.78	$4.8 \pm 1.3$	$(2.8_{-0.7}^{+0.7}) \times 10^{37}$
2004 Nov 01	4736	77.35	$2.3 \pm 0.6$	$(1.3_{-0.3}^{+0.3}) \times 10^{37}$
2004 Nov 07	6152	44.09	$1.2 \pm 0.7$	$(0.7_{-0.4}^{+0.4}) \times 10^{37}$
2004 Dec 22	6170	47.95	$8.3 \pm 1.3$	$(4.1_{-0.7}^{+0.7}) \times 10^{37}$
2004 Dec 24	6175	40.66	$13.1 \pm 1.8$	$(7.0_{-1.0}^{+1.0}) \times 10^{37}$
2004 Dec 30	6169	29.38	$210 \pm 8$	$(7.4_{-0.4}^{+0.7}) \times 10^{38}$
2005 Jan 01	4737	21.85	$664 \pm 17$	$(1.6_{-0.1}^{+0.1}) \times 10^{39}$
2005 Jan 08	0212480201	13.7	$447 \pm 15$	$(4.6_{-0.2}^{+0.2}) \times 10^{38}$

**Table 1.** Log of the observations considered for this study, and net count rate in the 0.3–2 keV band.  $L_{0.3-10}^{\min}$  is the inferred 0.3–10 keV luminosity (defined as  $4\pi d^2 \times$  observed flux) corrected *only* for the line-of-sight Galactic absorption  $n_{\text{H}} = 1.5 \times 10^{20}$  cm $^{-2}$ ; this is a strong, almost model-independent lower limit to the bolometric luminosity. Errors are 68% confidence limits. All the entries in this table are *Chandra*/ACIS observations, except for 2004 July 23 and 2005 January 8, which are *XMM-Newton*/EPIC observations. The net count rate for those two observation is the combined rate of pn, MOS1 and MOS2.

of the inner disk emission in a warm ( $kT_e \sim 2$ keV), optically thick corona (Middleton et al. 2015; Mukherjee et al. 2015; Walton et al. 2015; Roberts 2007); the softer emission might come from a radiatively driven outflow, launched near or just outside the spherization radius (King & Pounds 2003; Poutanen et al. 2007; Sutton et al. 2013; Middleton et al. 2015), or also from the disk (Miller et al. 2013). The broad-band continuum becomes steeper, with a characteristic downturn at lower energies ( $E \approx 5$  keV) for sources seen at higher inclination angles, probably because the X-ray

photons in our line of sight pass through and are down-scattered by a thicker disk wind (soft ultraluminous regime: Sutton et al. 2013). Instead, ULXs seen at low inclination angles have a harder spectrum (hard ultraluminous regime), consistent with the interpretation that higher-energy photons emitted in the innermost part of the inflow can emerge from the low-density polar funnel with less downscattering. This scenario is consistent with numerical and theoretical models of massive radiatively-driven outflows in the super-

critical regime (Poutanen et al. 2007; Dotan & Shaviv 2011; Ohsuga & Mineshige 2011; Kawashima et al. 2012).

Two rare subclasses of ULXs remain hard to explain with the super-Eddington stellar-mass BH scenario. The first case is that of “hyperluminous” X-ray sources, that is those very few ULXs (most notably, ESO 243–49 HLX-1: Farrell et al. 2009, and M82 X41.4+60: Feng & Kaaret 2010; Pasham et al. 2014) that reach  $L_X \gtrsim 10^{41}$  erg s<sup>-1</sup>, two orders of magnitude higher than the Eddington limit of an ordinary  $10M_\odot$  BH. For those sources, an intermediate-mass BH with  $M > 100M_\odot$  is the most likely explanation. The hyperluminous subclass is outside the scope of this work.

The second unexplained subclass, which we discuss in this paper, is that of “supersoft” ULXs (Di Stefano & Kong 2003), henceforth referred to as ultraluminous supersoft sources (ULSs). A purely empirical definition of ULS is a source that is dominated by soft, blackbody-like emission with a hardness ratio (M–S)/T  $\lesssim -0.8$  (where S, M and T are the *Chandra* or *XMM-Newton* count rates in the 0.3–1.1 keV, 1.1–2.5 keV and 0.3–7.0 keV bands), and that has reached an extrapolated bolometric luminosity of the thermal component  $L_{\text{bol}}^{\text{bb}} \gtrsim 10^{39}$  erg s<sup>-1</sup> in at least one observation. The best-known representatives of this group have been detected in M101 (Kong et al. 2004; Kong & Di Stefano 2005; Mukai et al. 2005; Liu 2009; Liu et al. 2013), M81 (Swartz et al. 2002; Liu & Di Stefano 2008; Liu 2008), M51 (Di Stefano & Kong 2003; Terashima & Wilson 2004), NGC 300 (Read & Pietsch 2001; Kong & Di Stefano 2003), NGC 4631 (Vogler & Pietsch 1996; Carpano et al. 2007; Soria & Ghosh 2009), NGC 247 (Jin et al. 2011; Tao et al. 2012) and the Antennae (Fabbiano et al. 2003). A detailed study of the common properties of this whole group of ULSs is presented in a companion paper (Urquhart & Soria 2015). In this paper, instead, we focus mostly on the M101 ULS (often referred to in the literature as M101 ULX-1 or CXO J140332.3+542103), which has arguably the most extensive X-ray coverage among the ULS population.

The dominant thermal component of ULS spectra has colour blackbody temperatures  $kT_{\text{bb}} \approx 50\text{--}150$  eV (hence, very little emission  $> 1$  keV), often varying from observation to observation. The characteristic blackbody radii are  $R_{\text{bb}} \approx 10,000\text{--}100,000$  km. Blackbody-model bolometric luminosities reach  $\approx$  a few  $10^{39}$  erg s<sup>-1</sup>, although for such low temperatures, luminosity estimates have to be taken with great caution. It is well known (Kahabka & van den Heuvel 1997; Balman et al. 1998; Greiner 2000; Ness et al. 2008) that in Local Group supersoft sources, simple blackbody fits tend to overestimate the bolometric luminosity and underestimate the temperature, compared with white dwarf atmosphere models. It was also recently found (Ness et al. 2013), via X-ray grating spectroscopy, that the spectra of Local Group supersoft sources are far richer in absorption and emission lines than previously thought. Unfortunately, for extragalactic ULSs, the count rate is too low for grating spectroscopy, and their physical properties have to be inferred from CCD-resolution spectroscopy.

Several models have been proposed for ULSs. One suggestion (Kong & Di Stefano 2003; Kong et al. 2004; Liu & Di Stefano 2008) was that they are powered by intermediate-mass BHs (IMBHs) in a disk-dominated state. One problem of this scenario is that the observed colour temperatures are very low, often dipping below 100 eV. A stan-

dard disk reaches a peak temperature  $kT_{\text{in}} \approx 230(\dot{m}/M_4)^{1/4}$  eV (Done et al. 2012; Soria 2007; Kubota et al. 1998), where  $M_4$  is the BH mass in units of  $10^4 M_\odot$ . The corresponding luminosity is  $L \approx 1.3 \times 10^{42} \dot{m} M_4$  erg s<sup>-1</sup>. Usually, an accreting BH is in a disk dominated state only for  $0.02 \lesssim \dot{m} \lesssim 0.3$  (Maccarone 2003; Steiner et al. 2009) (canonical high/soft state), or more generally for  $0.02 \lesssim \dot{m} \lesssim 1$  if we also include the non-standard disk regime near the Eddington limit. Combining this limit on  $\dot{m}$  with the previous expressions for  $kT_{\text{in}}$  and  $L$ , it is easy to show that BHs are expected to be in a disk-dominated state only in a specific region of the temperature-luminosity plane, namely for

$$5.2 \times 10^{38} \left( \frac{230 \text{ eV}}{kT_{\text{in}}} \right)^4 \lesssim \frac{L}{\text{erg s}^{-1}} \lesssim 1.3 \times 10^{42} \left( \frac{230 \text{ eV}}{kT_{\text{in}}} \right)^4. \quad (1)$$

As discussed in a companion paper (Urquhart & Soria 2015), ULSs fall mostly outside of that region of parameter space. Therefore, a disk-dominated IMBH model is in most cases not self-consistent, although we cannot rule out the IMBH scenario a priori for all sources.

Alternatively, ULSs are extreme examples of quasi-steady surface-nuclear-burning white dwarfs in close binary systems, by analogy with (less luminous) supersoft sources in the Milky Way and Local Group (van den Heuvel et al. 1992; Rappaport et al. 1994; Greiner 2000; Greiner et al. 2004; Di Stefano & Kong 2004; Orío et al. 2010). The characteristic blackbody radii of ULSs are a few times larger than white dwarf radii. However, that is not inconsistent with the accreting white dwarf scenario: as the luminosity produced by shell burning reaches and exceeds the Eddington limit for a white dwarf ( $L \approx 10^{38}$  erg s<sup>-1</sup>), we do expect envelope expansion and/or an optically thick outflow (Hachisu et al. 1996; Fabbiano et al. 2003). Recurrent novae (also powered by nuclear burning on an accreting white dwarf) are known to exceed the Eddington limit in their outbursts: RS Oph reached  $L \approx 10^{40}$  erg s<sup>-1</sup> and remained super-Eddington for at least two months during its 2006 outburst (Skopal 2015a,b).

A third explanation for ULSs is that they are stellar-mass BHs or neutron stars accreting strongly above their Eddington limit, so that the central X-ray source is completely shrouded by a massive radiatively-driven outflow. The X-ray photons from the inner disk are downscattered and thermalized in the Compton-thick wind, and we are seeing the photosphere of the outflow (Mukai et al. 2003; King & Pounds 2003; Fabbiano et al. 2003; Poutanen et al. 2007; Shen et al. 2015). Mildly super-Eddington accretion is now the generally accepted explanation for the vast majority of standard ULXs. In this scenario, ULSs are the extreme end of the general ULX population, when viewed through the thickest winds (corresponding to a combination of highest accretion rates and sufficiently high viewing angle).

Recent multiband studies of the M101 ULS (Liu et al. 2013) seemed to provide the solution for the nature of ULSs. However, such results have also posed some new unanswered questions: in particular, whether or not the soft emission is coming from a standard accretion disk, and if so, why it is so cold. In this paper, we discuss whether there is an alternative interpretation, that can better explain its X-ray spectral properties and high luminosity.

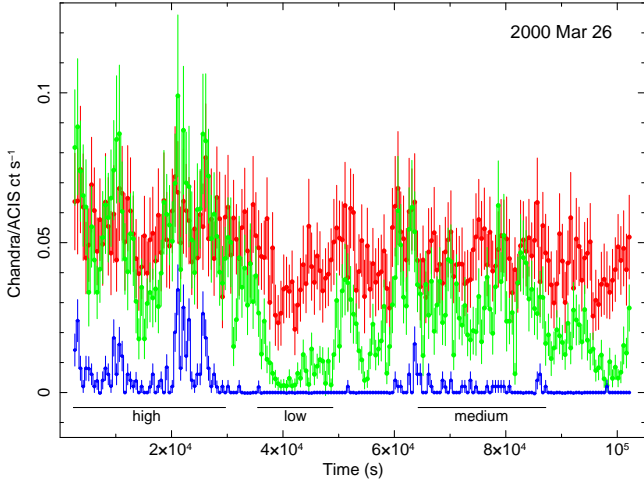


**Figure 1.** *Chandra*/ACIS-S lightcurve of the M 101 ULS in the 0.3–0.7 keV (red datapoints), 0.7–1.5 keV (green datapoints) and 1.5–7 keV (blue datapoints) bands, in the 2000 March 26 observations, rebinned to 500s intervals. We also show the “high”, “medium” and “low” sub-intervals previously defined and modelled by Mukai et al. (2003); Kong & Di Stefano (2005). We use the same three sub-intervals in our spectral analysis, for a better comparison with the literature results.

## 2 THE ULS IN M 101: A CHALLENGE TO STANDARD DISC MODELS

The *Chandra* position of the M 101 ULS is R.A. =  $14^{\text{h}}03^{\text{m}}32^{\text{s}}.37$ , Dec. =  $+54^{\circ}21'02''.8$ . Henceforth, we assume a Cepheid distance of 6.4 Mpc to M 101 (Shappee & Stanek 2011:  $d = 6.4 \pm 0.2$  (random)  $\pm 0.5$  (systematic) Mpc). For comparison, a distance of 6.9 Mpc (Freedman et al. 2001) was instead adopted by Liu et al. (2013). From their optical spectroscopic study, Liu et al. (2013) concluded that the M 101 ULS contains a BH with mass  $M_{\text{BH}} > 5M_{\odot}$ , accreting from a Wolf-Rayet star of current mass  $M_2 = (19 \pm 1)M_{\odot}$  (initial mass  $M_{2,0} = (50 \pm 10)M_{\odot}$ ), in a binary system with orbital period  $P = 8.24 \pm 0.1$  days. With these parameters, the donor star is underfilling its Roche lobe: as a result, the system must be powered by wind accretion. In turn, this poses severe lower limits to the BH mass, in order for enough mass to be intercepted by the BH ( $M_{\text{BH}} \gtrsim 50M_{\odot}$  for a non-spinning BH). In such conditions, the M 101 ULS cannot be a persistently super-Eddington source: in Liu et al. (2013)’s model, the accretion rate reaches only  $\approx 10^{-7}M_{\odot} \text{ yr}^{-1}$ : this is barely viable if the long-term-average bolometric luminosity of the BH is  $\approx 3 \times 10^{38} \text{ erg s}^{-1}$ , as opposed to a luminosity  $\approx 3 \times 10^{39} \text{ erg s}^{-1}$  reached during bright states.

The supersoft thermal component is interpreted by Liu et al. (2013) as optically-thick disk emission, directly observed without any reprocessing in a hot corona. The main benefit of attributing the soft thermal emission directly to the disk is that this scenario can explain the luminosity variability between high- and low-flux epochs. The stellar wind itself cannot change by two orders of magnitude over few weeks; however, if accretion is mediated by a disk, thermal/viscous instabilities may give rise to the observed spectral transitions. This introduces two additional constraints on the BH mass. Firstly, the disk cannot form in a wind-

accreting system unless the circularization radius of the captured wind is larger than the innermost stable circular orbit: for this to occur, the BH mass must be  $M_{\text{BH}} \gtrsim 80M_{\odot}$  or  $M_{\text{BH}} \gtrsim 50M_{\odot}$ , depending on which stellar wind model is adopted (Liu et al. 2013). Secondly, a standard accretion disk is in the thermal dominant state only below  $\approx 30\%$  of the Eddington luminosity, *i.e.*,  $\dot{m} \lesssim 0.3$  (Fender et al. 2004; McClintock & Remillard 2006; Steiner et al. 2009). Coupled with the inferred bolometric luminosity in the bright states, this constraint on the Eddington ratio requires the BH mass to be  $M_{\text{BH}} \gtrsim 80M_{\odot}$ , possibly inconsistent with a stellar origin of the BH. Finally, no stellar-mass BH has ever been observed with a pure disk spectrum at temperatures  $< 0.1$  keV: as Liu et al. (2013) note, their own interpretation of this ULS challenges standard models of BH accretion and disk structure. Considering the unsolved problems of the disk scenario, it is worth re-examining alternative explanations for the supersoft thermal component, which we will discuss in this paper.

## 3 DATA ANALYSIS

M 101 has been observed by many X-ray missions over the years. For this paper, we have chosen to re-analyze the 25 *Chandra* observations, from 2000 March–October and 2004 January–2005 January, and the two *XMM-Newton* observations from 2004 July and 2005 January. All of them are available on their respective public archives. There is also another *XMM-Newton* observation from 2002 June in which the source is barely detected at  $3\text{-}\sigma$  level (Kong et al. 2004; Jenkins et al. 2004) but with insufficient signal-to-noise ratio to provide any useful spectral or colour information; therefore, we did not use the 2002 June observation in this paper. The ULS was also previously detected in three of the 12 *ROSAT*/High Resolution Imager observations taken between 1992 and 1996 (source H32 in Wang et al. 1999); however, the combined number of counts from those three (short) observations is only  $\approx 50$ . Therefore, a full re-analysis of the *ROSAT* data does not provide particularly useful additional information.

For *Chandra*, we re-processed the data with standard tasks in the CIAO Version 4.6 (Fruscione et al. 2006) data analysis system. In particular, we used the CIAO task *specextract* to extract a spectrum (with its associated background, response and ancillary response files) from each observation. In a few cases (Table 1), there are enough counts for a meaningful spectral modelling, and the observed count rate corresponds to X-ray luminosities  $\sim 10^{39} \text{ erg s}^{-1}$ . In most other cases, the ULS is barely detected at  $\sim 3\sigma$  level, corresponding to X-ray luminosities  $\sim 10^{37} \text{ erg s}^{-1}$ . We carried out individual spectral fitting for the data from ObsIDs 934, 2065, 4737, 6169. In fact, we split the long ObsID 934 (98 ks) into three intervals with high, medium and low observed count rates, defined exactly as in Mukai et al. (2003) and Kong & Di Stefano (2005), and fitted them individually. (The three sub-intervals are illustrated in Figure 1, and discussed in more detail in Section 4.1.) We combined and fitted the average spectrum from ObsIDs 4734, 5337, 5338, 5339 and 5340 (spanning the time range 2004 July 5–11, for a total exposure time of 143 ks), and the average spectrum from ObsIDs 6170 and 6175 (2004 December 22–24; 89 ks).

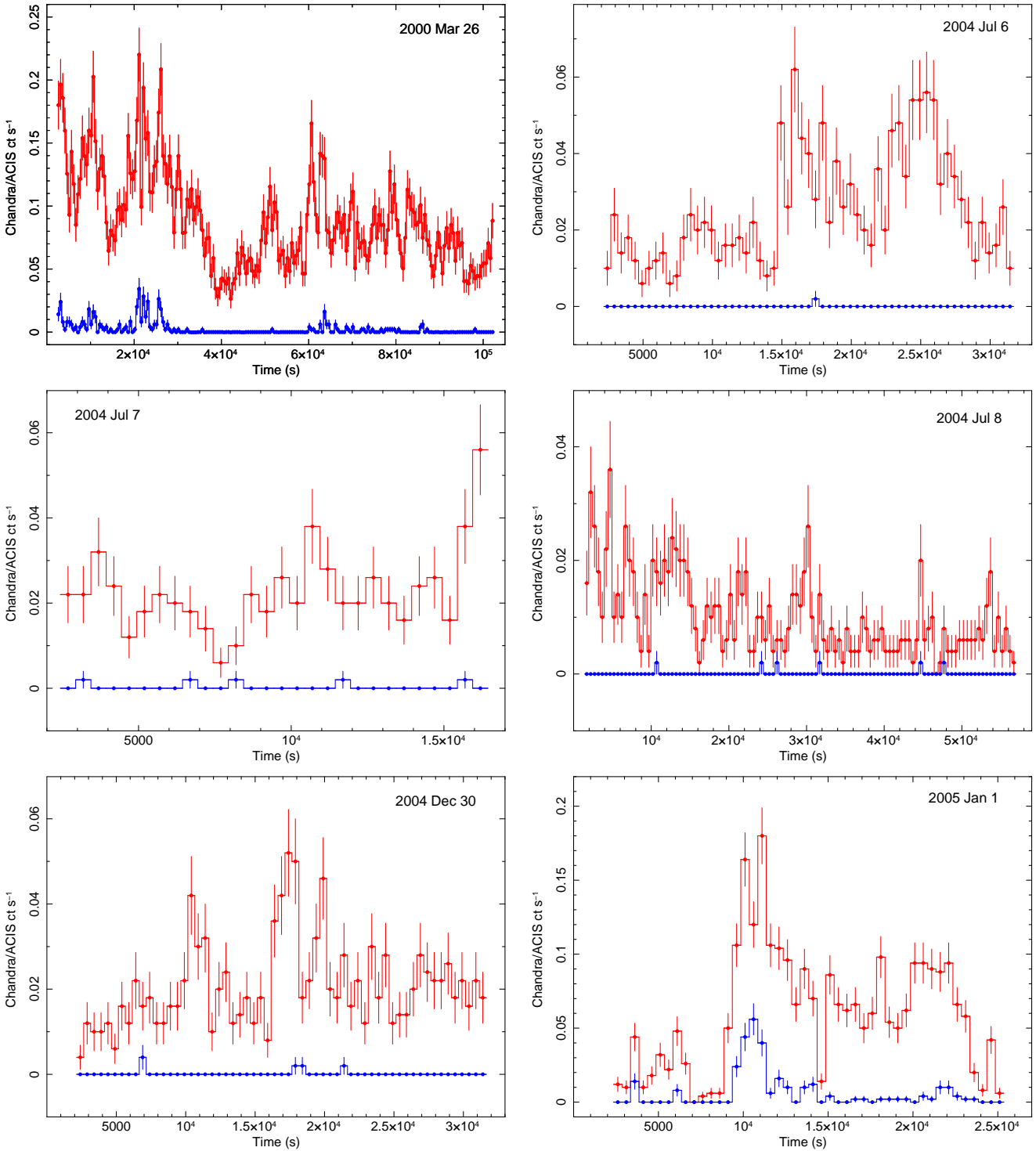


**Figure 2.** *Chandra*/ACIS-S lightcurve of the M101 ULS in the 0.3–1.5 keV band (red datapoints) and 1.5–7 keV band (blue datapoints), for selected observations. All lightcurves are rebinned to 500s intervals.

Finally, we produced and fitted a deep combined spectrum from the 14 “faint-state” observations in which the source had a 0.3–2 keV count rate  $< 5 \times 10^{-4}$  ct s $^{-1}$  (ObsIDs 4731, 5297, 5300, 5309, 4732, 5322, 4733, 5323, 6114, 6115, 6118, 4735, 4736 and 6152, for a total exposure time of 670 ks). All combined spectra were produced with *specextract*,

so that individual spectral and response files were created for each epoch and then averaged.

For both the *XMM-Newton* observations considered here, we reprocessed the Observation Data Files with the Science Analysis System (SAS) version 14.0.0 (xmm-sas\_20141104). For the 2004 July 23 observation, we had to

**Table 2.** Root-mean-square fractional variability in different energy bands, for selected observations with high signal-to-noise ratio.

Epoch	Frequency band (Hz)	rms (0.3–0.7 keV)	rms (0.7–1.5 keV)	rms (1.5–7.0 keV)
2000 Mar 26	$10^{-5}$ –0.05	< 36%	(70 ± 4)%	(100 ± 24)%
2000 Oct 29	$1 \times 10^{-4}$ –0.01	(31 ± 15)%	–	–
2004 Jul 06	$4 \times 10^{-5}$ –0.05	(41 ± 17)%	(76 ± 29)%	–
2004 Jul 08	$2 \times 10^{-5}$ –0.05	(102 ± 11)%	–	–
2004 Jul 11	$3 \times 10^{-5}$ –0.01	(50 ± 19)%	–	–
2004 Dec 30	$3 \times 10^{-5}$ –0.01	(22 ± 17)%	(63 ± 21)%	–
2005 Jan 01	$5 \times 10^{-5}$ –0.05	(58 ± 12)%	(89 ± 6)%	(162 ± 17)%
2005 Jan 08	$7 \times 10^{-5}$ –0.01	(27 ± 10)%	–	–

remove about 1/3 of the exposure time due to background flaring. We extracted the source events from a circular region centred on the ULS, with a 20" radius; we extracted the local background from a region three times as large, suitably selected to avoid any other bright sources or chip gaps. We selected single and double events (pattern  $\leq 4$  for the pn and pattern  $\leq 12$  for MOS1 and MOS2), with the standard flagging criteria #XMMEA\_EP and #XMMEA\_EM for the pn and MOS, respectively, and with the stricter flagging condition FLAG=0 for spectral analysis. We built response and ancillary response files with the SAS tasks *rmfgen* and *arfgen*, and we then created an average EPIC spectrum and response file with *epicspeccombine*. We grouped the combined spectrum to a minimum of 20 counts per bin, for  $\chi^2$  fitting. For the 2005 January 8 observation, we also fitted the pn and MOS spectra simultaneously, verifying that we obtained a result consistent with that obtained from the combined spectrum within the 90% confidence limit; for the 2004 July 23 observation, there are not enough counts in the MOS to permit simultaneous spectral fitting.

We used XSPEC Version 12.6 (Arnaud 1996) for spectral fitting, both for *Chandra* and *XMM-Newton*. For models involving pileup (see Section 4.3), we also double-checked the results with the spectral fitting package ISIS (Houck & Denicola 2000), and found them consistent within the 90% uncertainties. Both XSPEC and ISIS use independent implementations of a pile-up model developed by Davis (2001).

For the time variability study, we used the CIAO task *dmextract* to extract *Chandra* lightcurves in the soft (0.3–1.5 keV) and hard (1.5–7 keV) band. For the *XMM-Newton* observations, we used the SAS tasks *xmmselect* and *epiclccorr* to extract background-subtracted EPIC-pn and EPIC-MOS lightcurves. We then used standard FTOOLS tasks for timing analysis and statistics (Blackburn 1995).

## 4 RESULTS

### 4.1 Time variability

The most striking feature of the X-ray lightcurves at most epochs is their strong short-term variability (Figures 1,2), as already noted in the literature (Mukai et al. 2003; Kong & Di Stefano 2005). The observed flux often varies by a factor of 3 in  $\approx 10^3$  s. This is much faster than

any  $e$ -folding rise or decay timescale of transient Galactic X-ray binaries attributed to disk instabilities (typically,  $\gtrsim 1$  d). The root-mean-square (rms) fractional variability (Edelson et al. 2002; Markowitz 2003; Vaughan et al. 2003; Gierliński & Zdziarski 2005; Middleton et al. 2011) of the 0.3–1.5 keV lightcurve, for frequencies  $\leq 0.1$  Hz, is as high as (32 ± 3)% on 2000 March 26, (58 ± 10)% on 2004 July 6, (100 ± 10)% on 2004 July 8, and (71 ± 5)% on 2005 January 1. For the observations with the highest signal-to-noise ratio, we also computed the rms fractional variability separately for the 0.3–0.7 keV and 0.7–1.5 keV bands (Table 2). The behaviour of the source on 2000 March 26 and 2005 January 1 suggests that the rms variability increases at harder energies (Table 2).

Modelling the physical origin of this variability is beyond the scope of this paper. Here, we just compare the level of rms variability seen in the M 101 ULS with that seen in other accreting BHs. The observed rms variability  $\sim 30\%$ –100% is higher than in any canonical state of stellar-mass BHs (Belloni 2010), and certainly inconsistent with the disk-dominated high/soft state, when the rms is < 10%. This is another strong argument against an IMBH disk model for this ULS.

Instead, high rms variability (up to  $\sim 50\%$ ) and an increase in rms variability at higher energy bands are two characteristic properties of ULXs in the soft-ultraluminous regime (Middleton et al. 2011; Sutton et al. 2013; Middleton et al. 2015). This has been interpreted as due to variable obscuration of the hard inner-disk emission by a clumpy disk wind, for ULXs seen at high inclination angle. Based on this analogy, we speculate that the M 101 source and other ULXs might be an extreme case of the soft-ultraluminous regime. In this scenario, ULXs could be super-critical accreting sources in which a clumpy outflow almost completely masks and reprocesses the harder emission from the central regions. The outflow must have an even higher optical depth than in the soft-ultraluminous sources discussed by Sutton et al. (2013). We will outline a possible analytic model for such an outflow in Section 5.2.

In most epochs, there is either no significant detection in the hard band (1.5–7 keV), or it is consistent with a count rate  $\lesssim 10^{-4}$  ct s $^{-1}$ . Significant spikes in the hard flux are seen (Figures 1,2) during the strongest soft flares of ObsID 934 (2000 March 26) and ObsID 4737 (2005 January 1). On both occasion, the hard emission appears only when the X-ray source reaches count rates  $\gtrsim 0.1$  ct s $^{-1}$ . We will use

spectral analysis (Sections 4.2 and 4.3) to determine whether the count-rate variability is associated to real changes in the emission properties or (for example) to occultation. We will also discuss whether the hard flares are an additional physical component, or are the Wien tail of the supersoft thermal component, or are entirely due to photon pileup, which is known to be significant at count rates  $\gtrsim 0.1$  ct s $^{-1}$ .

#### 4.2 Optically-thick thermal continuum

All spectra are dominated (Figures 3,4 and Appendix A) by a soft thermal component with a characteristic temperature  $\lesssim 0.1$  keV, therefore with a peak flux at photon energies  $\lesssim 0.3$  keV, at the lowest energy range of the *Chandra*/ACIS-S and *XMM-Newton*/EPIC detectors. In addition, some spectra have additional harder emission detected at  $\sim 1$ –5 keV, contributing a few per cent of the total luminosity. The combined spectrum of the faint-state observations (bottom right panel in Figures 3,4) is dominated by a power-law-like component but it also has a significant supersoft peak, consistent with a temperature of  $\approx 50$  eV, thus emitting almost entirely below the *Chandra* band. The best-fitting simple power-law model for the stacked faint-state spectrum has  $\chi^2 = 39.8$  for 12 degrees of freedom, while adding an  $\approx 50$ -eV blackbody component significantly improves the fit down to  $\chi^2 = 9.8$  for 10 degrees of freedom. In this section, we discuss our interpretation of the supersoft thermal continuum, which is the main focus of this work. In Section 4.3, we will discuss evidence and interpretations for the harder components.

Because of the very low temperature of the thermal emission, we find (unsurprisingly) that it is impossible to distinguish between a disk-blackbody and a single-temperature blackbody model. We are seeing only the Wien part of the thermal spectrum, which is almost identical in the two models. The only difference is that for each spectrum, the fitted colour temperature in the disk-blackbody model is slightly higher than the corresponding simple blackbody temperature (cf. Tables 3 and 4, and Model 4 versus Model 5 in Table A1), because of the slightly different way temperatures and normalization are defined in the two models. We verified that blackbody and disk-blackbody models are statistically equivalent for every epoch. For the rest of the paper, unless specifically indicated, we will use radii and temperatures from the blackbody fits, to allow a direct comparison with the outflow model.

Our fits show that the bolometric luminosity is always  $\gtrsim 2 \times 10^{39}$  erg s $^{-1}$  except for the faint state (Tables 3, 4). In the faint state, the extremely low temperature of the soft component makes it impossible to estimate a reliable bolometric luminosity (most of the emission being in the far-UV), but we cannot rule out (Table 3) that it is also consistent with  $\gtrsim 2 \times 10^{39}$  erg s $^{-1}$ . In fact, despite the huge differences (three orders of magnitude) in the observed X-ray count rates, all observations are consistent with a blackbody bolometric luminosity varying only within a small range of values, between  $\approx 3$ –10  $\times 10^{39}$  erg s $^{-1}$ . We have already mentioned (Section 1) that such bolometric extrapolations in supersoft sources may overestimate the true luminosity. Even if that is the case, the general significance of our result is that the large difference in X-ray count rates between “bright” and “faint” states is mostly due to changes in the

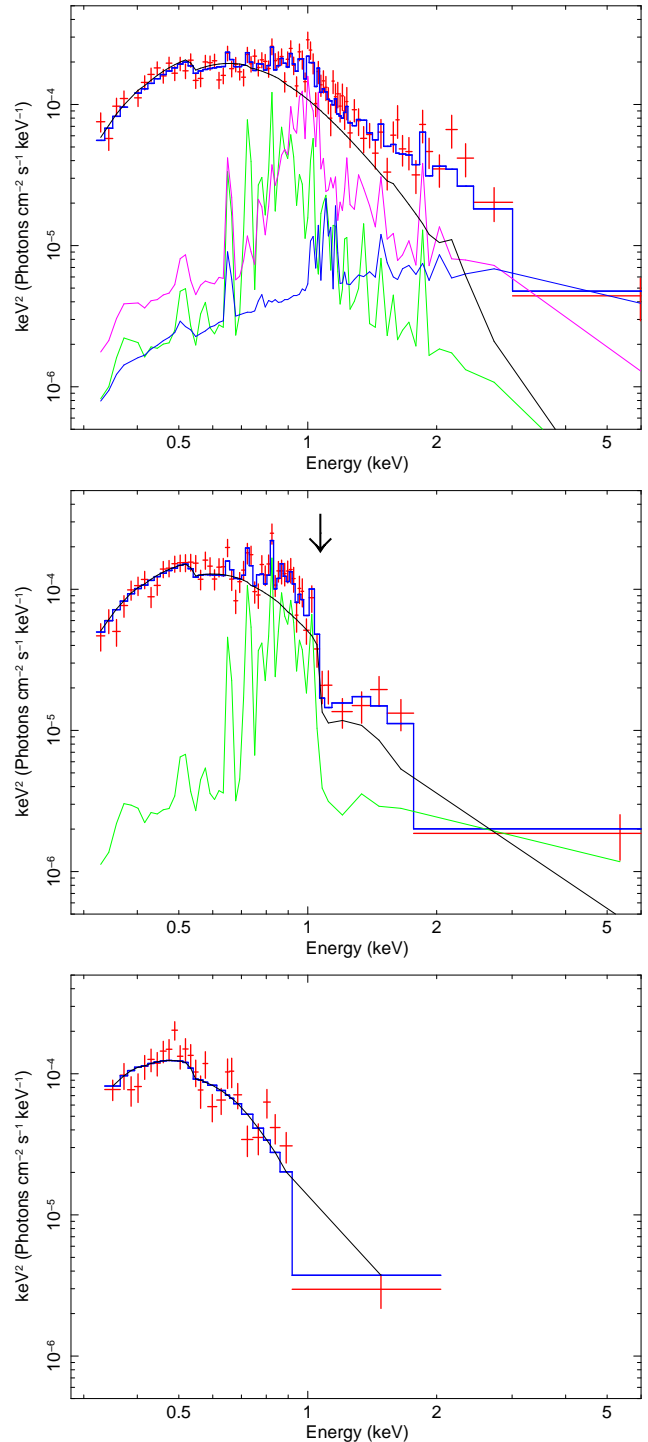


**Figure 5.** Unfolded spectra and model components for the *Chandra* ObsID 934, split into high, medium- and low-count-rate sub-intervals (as defined in Figure 1; see also the top left panel of Figures 3,4). The absorbing column density and the temperatures (but not the normalizations) of the three *mekal* components were kept locked for the three sub-intervals. See Table A2 for the best-fitting parameters. Top panel: the spectrum from the high-count-rate interval has three significant *mekal* components in addition to the soft blackbody. Middle panel: the medium-count-rate spectrum has only one significant *mekal* component, but it has an absorption edge (marked by the black arrow). Bottom panel: the low-count-rate spectrum is well fitted by a simple absorbed blackbody, with no hard excess or other residuals.

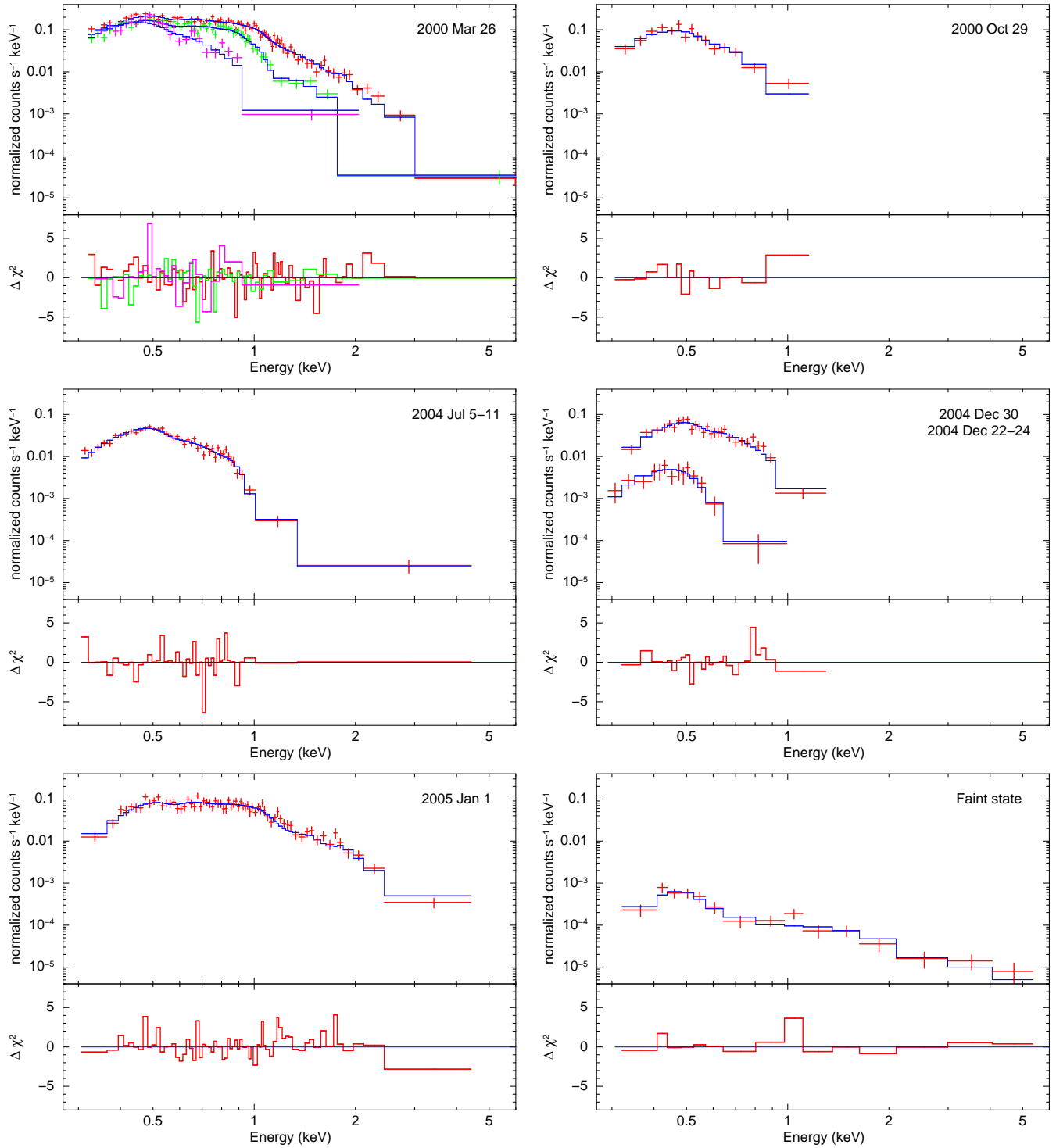


**Figure 3.** *Chandra*/ACIS-S spectral data and  $\chi^2$  residuals at different epochs. The full set of model components and parameters used for these plots are listed in Tables A2 (for ObsID 934 = 2000 March 26), and Table A4 (for all other epochs). The best-fitting parameters of the dominant blackbody component at each epoch are also summarized in Table 3. Datapoints have been binned to  $> 15$  counts per bin. For ObsID 934 (top left panel), we split the spectrum into a high-count-rate (red datapoints and residuals), medium-count-rate (green) and low-count-rate (magenta) sub-intervals. We did not plot the residuals from the stacked observations of 2004 December 22–24 because the corresponding fit was obtained with the Cash statistics rather than with  $\chi^2$ ; the stacked spectrum of 2004 December 22–24 was then rebinned to a signal-to-noise ratio  $\geq 2$  for display purposes only.

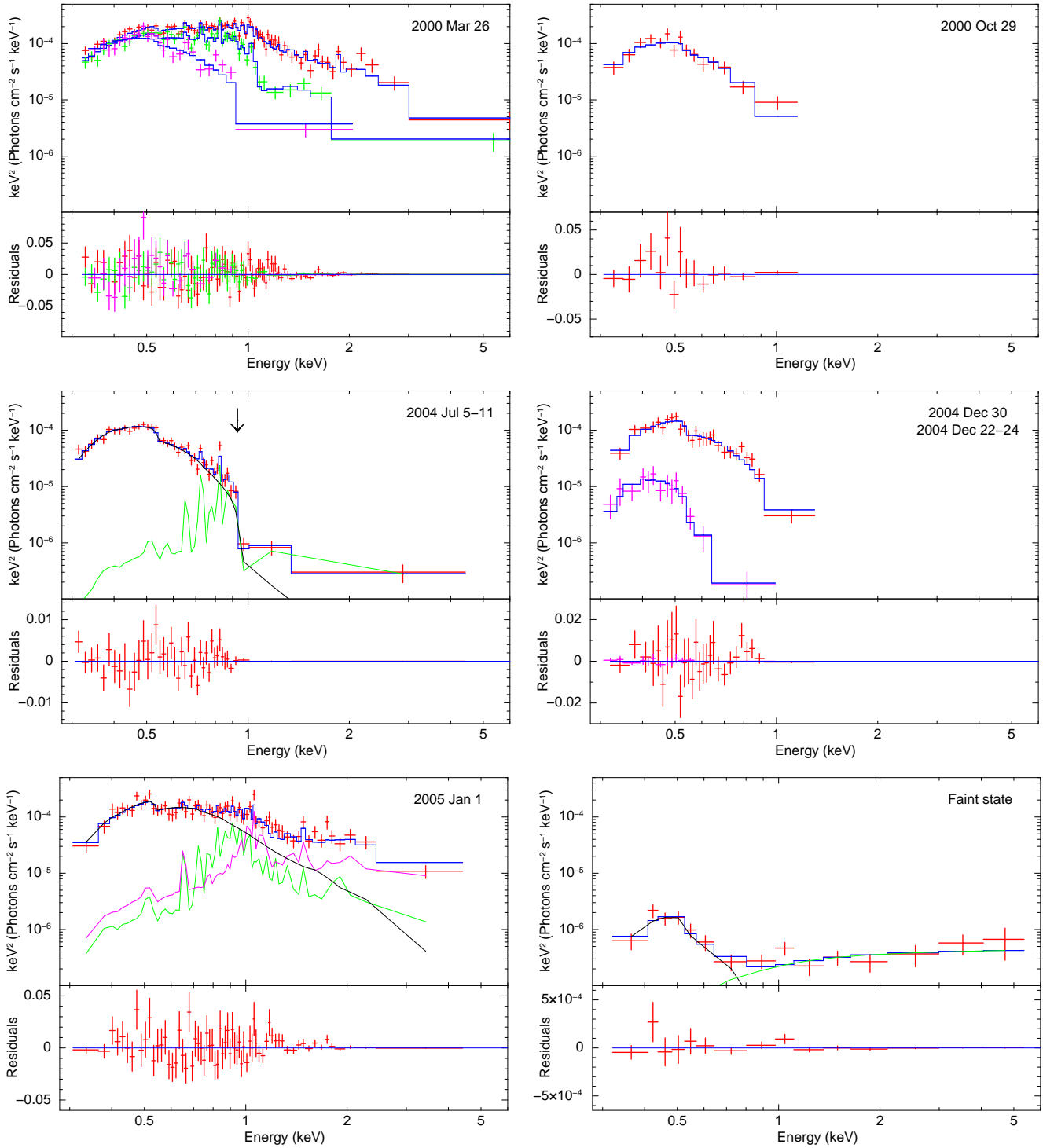


**Figure 4.** Same set of *Chandra*/ACIS-S spectra as shown in Figure 3, but this time plotted as unfolded spectra (*ceuf* in XSPEC, corresponding to units of  $\nu f_\nu$ ) and count-rate residuals. When the best-fitting model includes multiple components, they are also plotted in each panel, except for the 2000 March 26 spectrum (top left panel) which is expanded for clarity in Figure 5. An absorption edge in the stacked 2004 July 5–11 spectrum (middle row, left panel) is marked with a black arrow. The full set of model parameters corresponding to these plots are listed in Tables A2, A4. Datapoints have been binned to  $> 15$  counts per bin.

blackbody temperature, causing the thermal component to slip out of the detector sensitivity. We suggest that this is analogous to the well-documented behaviour of some classical supersoft sources, which can switch between a UV-bright phase (when the optically-thick envelope expands and cools) and an X-ray-bright phase (when the radius of the envelope decreases and its photospheric temperature increases) (van den Heuvel et al. 1992; Pakull et al. 1993). We find no significant trend of the bolometric luminosity versus fitted temperature or radius, which is to say that  $R_{\text{bb}}$  roughly scales as  $T_{\text{bb}}^{-2}$  (as shown in more details in Section 5.3).

### 4.3 Hard component and edges

A harder X-ray excess is detected in several epochs, with different properties. The stacked dim state is the only X-ray spectrum dominated by hard emission (Figure 2, bottom right panel). Fitting it with a thermal component plus power-law, we obtain a photon index  $\Gamma = 1.9^{+0.9}_{-0.7}$  and an unabsorbed 0.3–10 keV flux in the power-law component  $f_{\text{pl}} \approx 2 \times 10^{-15}$  erg cm $^{-2}$  s $^{-1}$ , corresponding to an emitted power-law luminosity  $L_{\text{pl}} \approx 10^{37}$  erg s $^{-1}$ . The observed photon count rate due to the power-law component above 1 keV is only  $\approx 10^{-4}$  ct s $^{-1}$ ; the count rate above 1.5 keV is  $\approx 5 \times 10^{-5}$  ct s $^{-1}$ . There are not enough counts to attempt any physical interpretation of this component (*e.g.*, whether it is inverse-Compton emission, or synchrotron, or bremsstrahlung). We re-fitted all the spectra taken in brighter epochs, adding a constant power-law component with the same slope and normalization determined in the dim state. We find that such faint component may have been present at all epochs but would not be significantly detected in the spectra of any of them. The 1.5–7 keV model count rate in the stacked dim state is also consistent with the very low hard-band count rate detected in the lightcurves at most epochs (Figure 2). Therefore, we cannot say that the hard component appeared or strengthened in the dim state (as is the case instead in X-ray binaries, when they move from the high/soft to the low/hard state): it could have been always present but be detectable only when the supersoft thermal component slipped out of the *Chandra* energy band, and only thanks to the very deep exposure time of the stacked dim-state observation (670 ks).

A different (stronger) type of hard component is detected at some other epochs. This harder emission is most apparent in the two observations (2000 March 26 and 2005 January 1) taken when the source was brightest. We have already shown (Figures 1,2 and Table 2) that the harder emission has significant short-term variability, and hard-band flares often coincide with peaks in the soft-band count rate. Here, we investigate the harder emission further, focussing on its spectral properties.

The first possible explanation for the hard component is pile-up, as suggested by Kong & Di Stefano (2005). From the observed count rate and fitted parameters of the soft component, we used PIMMS Version 4.7b<sup>1</sup> to estimate that the average pile-up fraction is  $\approx 10\%$  for ObsID 934, and  $\approx 7\%$  for ObsID 4737. When we split ObsID 934 into three sub-intervals at high, medium and low count rates, we find a pile-

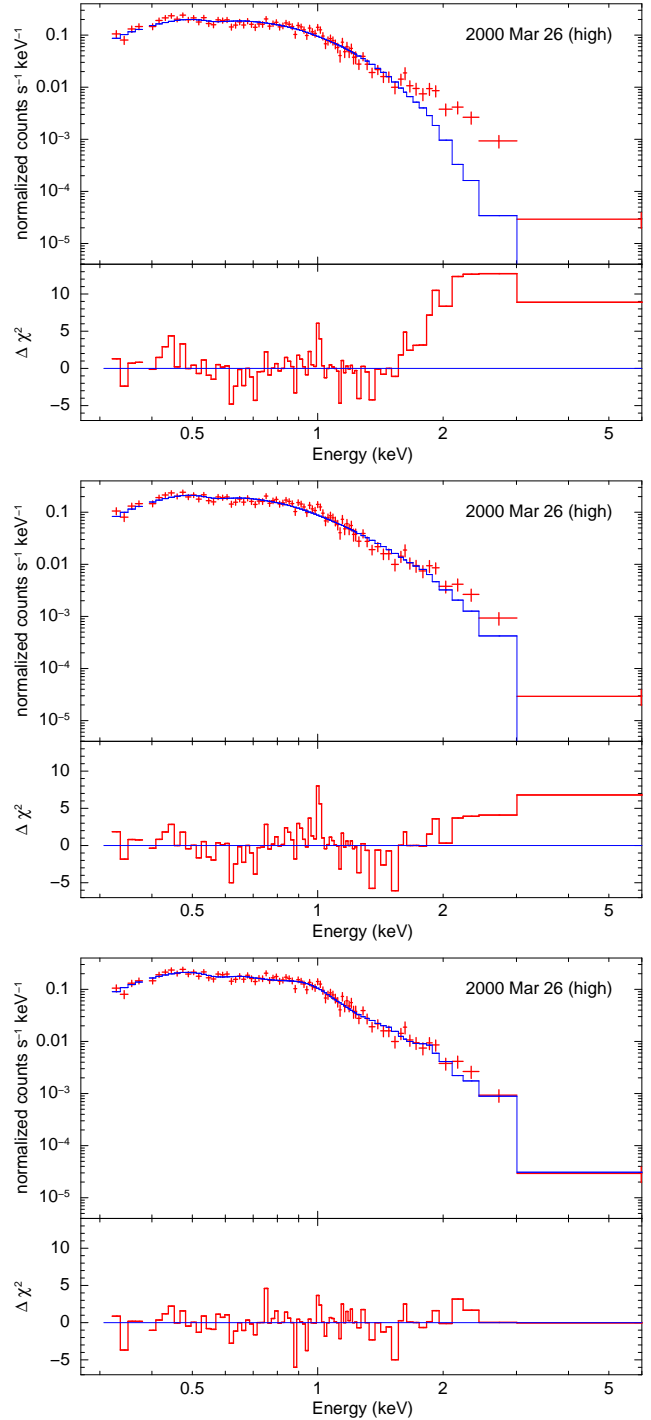


**Figure 6.** *Chandra*/ACIS-S spectral data and  $\chi^2$  residuals for the high-count-rate interval of ObsID 934, fitted with three different models. Top panel: absorbed single-temperature blackbody, showing a significant excess  $> 1.5$  keV (Model 1 in Table A1;  $\chi^2_{\nu} = 176.2/79$ ). Middle panel: absorbed single-temperature blackbody convolved with a pileup model; although some of the hard photons are now accounted for, the shape of the model is still unsatisfactory (Model 2 in Table A1;  $\chi^2_{\nu} = 128.7/78$ ). Bottom panel: absorbed piled-up blackbody plus two-temperature thermal plasma emission (*mekal* model), providing a significantly better fit with  $\chi^2_{\nu} = 84.9/74$  (Model 4 in Table A1). Datapoints have been binned to  $> 15$  counts per bin before fitting.

<sup>1</sup> <http://xc.harvard.edu/toolkit/pimms.jsp>

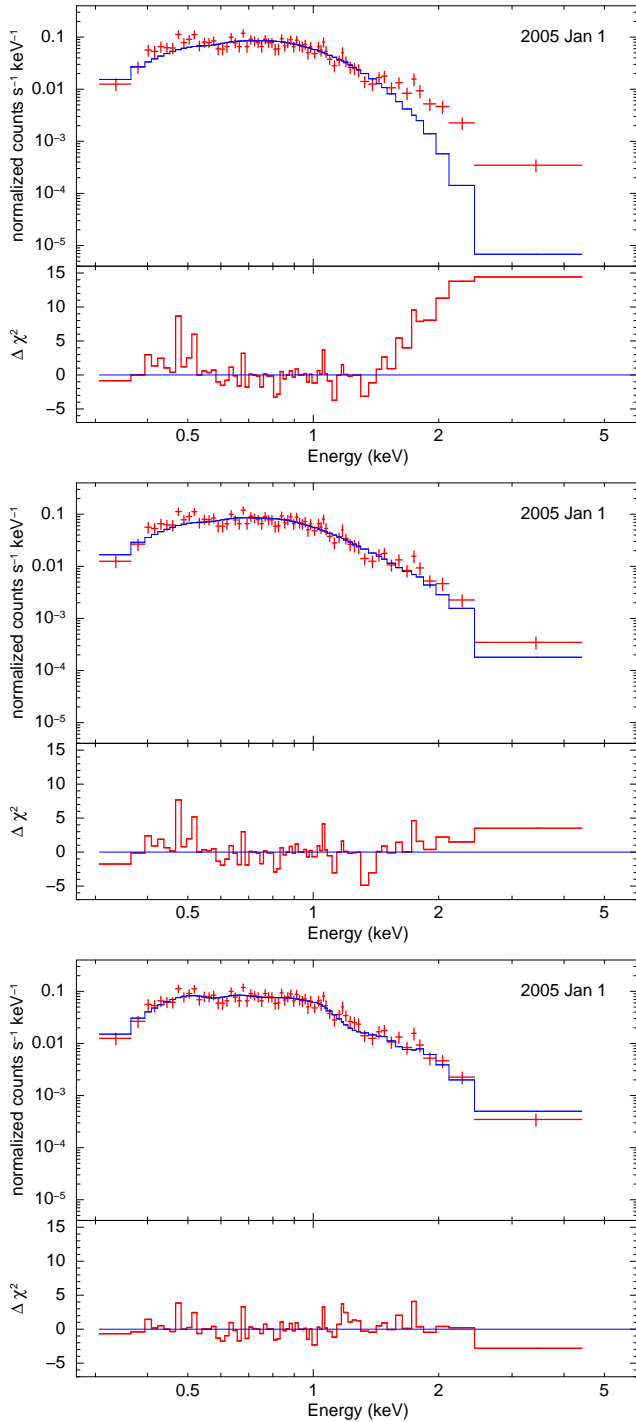


**Figure 7.** *Chandra*/ACIS-S spectral data and  $\chi^2$  residuals for ObsID 4737. Top panel: a simple blackbody does not provide an acceptable fit ( $\chi^2_{\nu} > 2$ ). Middle panel: correcting for pile-up improves the fit, giving  $\chi^2_{\nu} = 87.3/65$ ; however, systematic residuals are still clearly visible in the shape of the fitted spectrum. Adding a single-temperature thermal-plasma component (not shown) improves the fit to  $\chi^2_{\nu} = 79.8/63$ . Bottom panel: blackbody model with pileup and two-temperature thermal plasma, giving  $\chi^2_{\nu} = 63.5/61$ . This is a significant improvement of the fit at the 99% confidence level over a single-temperature thermal plasma model and over a model with no thermal plasma emission. See Table A4 for the value of the best-fitting parameters. Datapoints have been binned to  $> 15$  counts per bin before fitting.

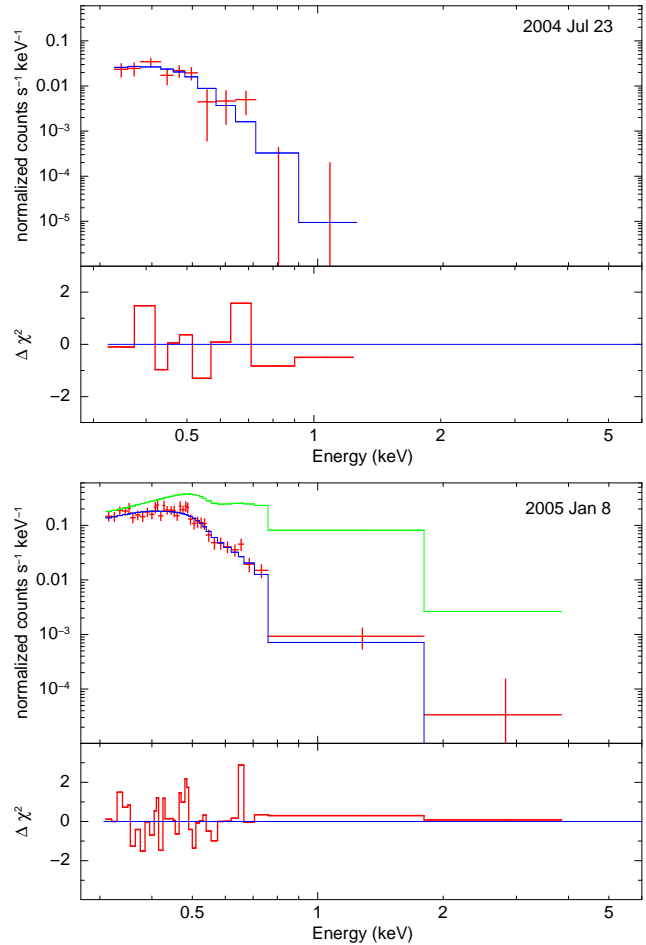


**Figure 8.** Top panel: *XMM-Newton*/EPIC spectral data and  $\chi^2$  residuals for the 2004 July 23 observation, fitted with an absorbed blackbody model. Bottom panel: *XMM-Newton*/EPIC spectral data and  $\chi^2$  residuals for the 2005 January 8 observation, fitted with an absorbed blackbody model. The green histogram is the count rate that would have been observed in the same binned channels if the spectrum was identical to that observed in the *Chandra* ObsID 4737 (*i.e.*, one week earlier): the harder tail has completely disappeared. The best-fitting parameters for both observations are listed in Table A5. Datapoints have been binned to  $> 20$  counts per bin before fitting.

up fraction as high as  $\approx 15\%$  in the brightest interval, and negligible in the faintest one. Therefore, we know that pile-up is likely to affect the spectral appearance to some degree. We convolved our blackbody model with pile-up models in XSPEC and ISIS and found that we can explain *some* of the hard emission in the bright state, as already shown by Kong & Di Stefano (2005). However, we cannot explain all of it, and we still see systematic residuals in the spectral shape (top and middle panels of Figures 6 and 7 for ObsID 934-high and ObsID 4737, respectively).

For the high-count-rate interval of ObsID 934, the best-fitting piled-up blackbody model (Model 2 in Table A1, plotted in the middle panel of Figure 6) provides a still unsatisfactory  $\chi^2_{\nu} = 128.7/78$ . Adding a *mekal* component (Model 3 in Table A1) dramatically improves the fit, giv-

Epoch	$R_{\text{bb}}$ ( $10^3$ km)	$kT_{\text{bb}}$ (eV)	$L_{\text{bb}}^{\text{bol}}$ ( $10^{39}$ erg s $^{-1}$ )
2000 Mar 26 (H)	$10.2^{+0.4}_{-0.3}$	$135^{+3}_{-4}$	$4.6^{+0.2}_{-0.3}$
2000 Mar 26 (M)	$10.5^{+0.3}_{-0.3}$	$119^{+3}_{-3}$	$2.9^{+0.2}_{-0.2}$
2000 Mar 26 (L)	$18.4^{+0.9}_{-1.0}$	$90^{+3}_{-3}$	$2.9^{+0.3}_{-0.3}$
2000 Oct 29	$29.0^{+32.7}_{-14.4}$	$77^{+11}_{-10}$	$3.6^{+6.8}_{-2.0}$
2004 Jul 5–11	$47.0^{+32.6}_{-17.0}$	$69^{+7}_{-7}$	$6.6^{+5.9}_{-2.9}$
2004 Jul 23	$64.7^{+*}_{-54.1}$	$48^{+20}_{-25}$	$3.5^{+*}_{-3.3}$
2004 Dec 22–24	> 54	< 49	> 2.1
2004 Dec 30	$43.5^{+29.3}_{-17.2}$	$75^{+6}_{-6}$	$7.7^{+8.6}_{-3.8}$
2005 Jan 1	$22.5^{+10.3}_{-4.7}$	$100^{+13}_{-10}$	$6.6^{+1.2}_{-1.0}$
2005 Jan 8	$101.5^{+82.7}_{-43.1}$	$56^{+5}_{-5}$	$12.8^{+17.9}_{-6.9}$
Faint state	$24.3^{+102.1}_{-10.8}$	$53^{+8}_{-11}$	$0.6^{+2.7}_{-0.2}$

**Table 3.** Physical parameters of the supersoft thermal component in various epochs, fitted with a single-temperature blackbody model. Errors are 90% confidence limits. See Tables A2, A4, A5 for the full set of spectral parameters in those fits. The stacked “faint state” spectrum is defined as explained in Section 3; the 2000 March 26 observation is split into high (H), medium (M) and low (L) count-rate sub-intervals.

Epoch	$r_{\text{in}} \sqrt{\cos \theta}$ ( $10^3$ km)	$kT_{\text{in}}$ (eV)	$L_{\text{diskbb}}^{\text{bol}} \times \cos \theta$ ( $10^{39}$ erg s $^{-1}$ )
2000 Mar 26 (H)	$5.9^{+0.3}_{-0.3}$	$174^{+6}_{-7}$	$4.1^{+0.2}_{-0.2}$
2000 Mar 26 (M)	$4.3^{+0.2}_{-0.2}$	$178^{+2}_{-2}$	$2.4^{+0.2}_{-0.2}$
2000 Mar 26 (L)	$13.0^{+1.1}_{-0.8}$	$109^{+2}_{-2}$	$3.1^{+0.4}_{-0.4}$
2000 Oct 29	$24.0^{+34.3}_{-12.3}$	$90^{+14}_{-13}$	$4.9^{+10.6}_{-2.8}$
2004 Jul 5–11	$39.7^{+30.4}_{-16.5}$	$81^{+9}_{-6}$	$8.5^{+7.1}_{-4.0}$
2004 Jul 23	$77.8^{+*}_{-70.3}$	$52^{+28}_{-34}$	$11.0^{+*}_{-10.5}$
2004 Dec 22–24	> 62	< 54	> 4.0
2004 Dec 30	$46.7^{+34.3}_{-12.3}$	$84^{+8}_{-6}$	$13.9^{+16.2}_{-7.5}$
2005 Jan 1	$8.6^{+14.9}_{-3.5}$	$147^{+6}_{-6}$	$4.4^{+7.9}_{-1.1}$
2005 Jan 8	$103.7^{+103.5}_{-44.6}$	$62^{+5}_{-5}$	$20.5^{+35.4}_{-10.5}$
Faint state	$24.5^{+128.3}_{-19.3}$	$59^{+8}_{-6}$	$1.0^{+16.6}_{-0.9}$

**Table 4.** Physical parameters of the supersoft thermal component in the same epochs listed in Table 2, but fitted with a disk-blackbody model. Errors are 90% confidence limits.

ing  $\chi^2_{\nu} = 93.4/76$  (an F-test significance<sup>2</sup> at the 99.999%

<sup>2</sup> Protassov et al. (2002) discuss caveats on the use of the F-test for the estimate of the significance of emission lines in X-ray spectra. We are aware of those caveats; however, we visually inspected our spectral fits with and without the additional absorption or emission features, and noticed clear systematic residuals when those components were not included.

level). Adding a second *mekal* component (Model 4 in Table A1, plotted in the bottom panel of Figure 6) further improves the fit, giving  $\chi^2_{\nu} = 84.9/74$ : the F-test shows that this is a significant improvement at the 97% level compared with the model with a single-temperature *mekal*. Adding a third *mekal* component to the fit does not lead to further significant improvements. However, when we fitted all three sub-intervals of ObsID 934 simultaneously (Table A2 and Figure 5), with locked *mekal* temperatures and column density, a third *mekal* component becomes significant in ObsID 934-high at the 98% level. The temperature range of the thermal-plasma components depends on whether we use a two-temperature or three-temperature approximation. Using a two-temperature *mekal* model, we find  $kT_1 \approx 0.7$  keV and  $kT_2 \approx 1.5$  keV; applying a three-temperature model, we find  $kT_1 \approx 0.6$  keV,  $kT_2 \approx 1$  keV and  $kT_3 \gtrsim 2$  keV. An equivalent interpretation of this finding is that ObsID 934-high has an extended hard-tail emission consistent with multi-temperature thermal-plasma emission, from  $kT \approx 0.6$  keV to  $kT \approx 2$  keV. For the medium-count-rate interval of ObsID 934 (Figure 5, middle panel), the addition of a single *mekal* component at  $kT \approx 0.6$  keV improves the piled-up blackbody fit with 99% significance; a second *mekal* component does not lead to any further significant improvements. Instead, the fit is dramatically improved (F-test significance > 99.999%) by adding an absorption edge at  $\approx 1.07^{+0.03}_{-0.05}$  keV (Figure 5, middle panel). Finally, ObsID 934-low (Figure 5, bottom panel) is well fitted with a simple (and cooler) blackbody spectrum, with no evidence of additional thermal plasma emission or edges.

Even a simple visual comparison of the spectral evolution between ObsID 934-high, ObsID 934-medium and ObsID934-low (top left panels of Figures 3,4, and Figure 5) strikingly confirms that the harder component is not just a marginal fitting residual or a pile-up artifact. The total unabsorbed 0.3–10 keV luminosity during ObsID 934-high is  $L_{0.3-10} \approx 4.3 \times 10^{39}$  erg s $^{-1}$ : of this, the contribution from the harder component is  $\approx 7 \times 10^{38}$  erg s $^{-1}$ , the rest coming from the  $\sim 0.1$ -keV optically thick blackbody emission. In ObsID 934-medium, the emission below  $\approx 1$  keV is approximately unchanged, but the harder flux has dramatically decreased; for example, an absorption edge appears to have replaced the higher-temperature thermal-plasma emission. In this regime, the thermal-plasma emission contributes just over  $\approx 10\%$  of the unabsorbed luminosity in the 0.3–10 keV band, that is  $\approx 3 \times 10^{38}$  erg s $^{-1}$ , compared with a total (supersoft blackbody plus harder components) 0.3–10 keV emitted luminosity of  $\approx 2.3 \times 10^{39}$  erg s $^{-1}$ . Finally, ObsID 934-low is well fitted with a simple (and cooler) blackbody spectrum, with a 0.3–10 keV emitted luminosity of  $\approx 1.5 \times 10^{39}$  erg s $^{-1}$  and no evidence of additional harder components or edges. In summary, within the single observation ObsID 934, the M101 ULS switched between a purely supersoft thermal state with  $kT_{\text{bb}} \approx 0.10$  keV, and a harder state with a broad-band tail detected at least up to 5 keV.

The other epoch when the M101 ULS spectrum displays a strong harder component is 2005 January 1 (ObsID 4737: bottom left panel of Figures 3,4). Adding a single-temperature *mekal* component provides a better fit than a piled-up blackbody model, with 95% significance; adding a second *mekal* component provides a further improvement with 99% significance (Figure 7). The best-fitting temper-

atures of the two components are  $kT_1 \approx 0.7$  keV and  $kT_2 \approx 1.3$  keV, consistent with the spread of temperatures modelled for Obs 934-high. The unabsorbed luminosity of the hard excess is  $\approx 7 \times 10^{38}$  erg s<sup>-1</sup>, again similar to the value estimated for Obs 934-high. Note that a week later, in the 2005 January 8 *XMM-Newton* observation, the hard tail had completely disappeared (Figure 8) and the blackbody component had cooled from  $\approx 100$  eV to  $\approx 50$  eV, while the fitted blackbody radius had increased from  $\approx 20,000$  km to  $\approx 100,000$  km.

ObsID 934 and ObsID 4737 have the highest observed count rates and highest 0.3–10 keV luminosities (Table 2), partly because the blackbody component is hotter in those two epochs, and partly because of their hard emission tails. Neither an excess hard component, nor an absorption edge is significantly detected in any other individual observation, as they are all consistent with a simple blackbody. However, we did find such features in the stacked spectrum from 2004 July 5–11 (Table 1 for the identification, and Table A4 for the fit parameters), because of the improved signal-to-noise ratio. A simple blackbody spectrum gives  $\chi^2_\nu = 61.3/41$ , while the fit improves to  $\chi^2_\nu = 42.3/37$  with the addition of a *mekal* component at  $kT \approx 0.6$  keV and an edge at  $E \approx 0.93$  keV (left middle panel in Figures 3,4). Both the *mekal* component and the edge are significant at the 99% confidence level. The unabsorbed luminosity of the hard excess is only  $\approx 3 \times 10^{37}$  erg s<sup>-1</sup>, which is why it is only significantly detected in the stacked spectrum. We summarize the energy and F-test significance of the excess emission and absorption components in Table 5.

It is important to remark here that a *mekal* (or an *apec*) model is the simplest but not the only option for fitting the excess harder emission. It provides a phenomenologically good tool at CCD resolution, with its moderately broadband emission peaking around 1 keV and not contributing much below  $\approx 0.5$  keV and above  $\approx 2$  keV. However, it is not necessarily the correct physical interpretation. For example, we verified that the non-equilibrium photo-ionization model *nei* also provides statistically equivalent fits. Thus, with the data at hand, we have no empirical elements to decide between collisionally ionized and photo-ionized gas.

Moreover, at moderately low signal-to-noise ratio and CCD spectral resolution, a phenomenological line-emission model can mimic a more physical model consisting of a smooth emission component above 1 keV (for example an inverse-Compton tail, or direct emission from the inner accretion disk) with a series of absorption edges (redshifted and blueshifted if the outflow is relativistic, as in the case of SS 433) imprinted by the dense outflow (Fabrika et al. 2007; Middleton et al. 2014). In fact, the fast variability of the hard excess, appearing and disappearing sometime within a few 1000 s, is more likely to be caused by variable occultation of an inner compact source of hard X-ray photons emerging through a clumpy wind. In this scenario, we speculate that the M101 ULS may have a pure supersoft blackbody spectrum when all the hard X-ray photons from the inner disk/corona are completely absorbed and reprocessed in an optically thick outflow; instead, it may show a harder tail at epochs when some of the hard X-ray emission emerges through the outflow (as is likely the case in the soft-ultraluminous regime of ULXs: Sutton et al. 2013; Middleton et al. 2015). The 2000 Mar 26 observation could

be an example of a transition between a ULS regime (blackbody component at  $kT_{\text{bb}} \approx 0.10$  keV and no hard tail), and a two-component soft-ultraluminous ULX regime. On the other hand, thermal plasma emission may also come from regions of the clumpy outflow that are just outside the photosphere, or when our line of sight is such that the outflow is not completely optically thick.

For ObsID 934-high, we tested whether an inverse-Compton component is consistent with the harder part of the emission tail. We replaced the higher temperature *mekal* component with a *comptt* component (Table A3), fixing its seed photon temperature  $kT_0$  equal to the blackbody temperature  $kT_{\text{bb}}$ . The electron temperature  $kT_e$  in the Comptonizing medium is not well constrained, because we do not have enough counts to detect a high-energy rollover; we arbitrarily fixed it at 4 keV, but any other choice of  $kT_e > 2$  keV does not change the results of the fit. The scattering optical depth  $\tau$  is  $> 2.0$ , but its upper limit is not constrained. Table A2 and A3 show that a Comptonization component provides as good a fit as a hot thermal plasma component.

Regardless of the uncertainty on the physical origin of the hard excess, we stress that the main objective of this paper is to compare the characteristic radii, temperature and bolometric luminosities of the supersoft component with the predictions of a phenomenological outflow model. The fitted values of such quantities are robust and not strongly dependent on the first-order corrections due to residual harder components.

## 5 DISCUSSION

### 5.1 The case against the accretion disk model

Both our timing and spectral results highlight severe problems for the disk interpretation. The strong short-term variability is clearly inconsistent with the typical behaviour of standard accretion disks in accreting BHs. If there is an accretion disk in the M101 ULs, it is clearly not in a steady state. More likely, the system is undergoing rapid flaring, more typical of fast outflows than of thermal or viscous processes inside a standard disk.

For a standard-disk emission spectrum, there is a fundamental relation between the inner radius  $R_{\text{in}}$ , the bolometric luminosity, and the peak temperature  $T_{\text{in}}$  (Shakura & Sunyaev 1973; Makishima et al. 1986; Kubota et al. 1998; Frank et al. 2002). Assuming that the disk extends down to the innermost stable circular orbit, this provides a rough BH mass estimate, which is empirically satisfied within a factor of 2 for Galactic stellar-mass BHs:

$$M \approx 10.0 \left( \frac{\eta}{0.1} \right) \left( \frac{\xi \kappa^2}{1.19} \right) \left( \frac{L_{\text{diskbb}}^{\text{bol}}}{5 \times 10^{38} \text{ erg s}^{-1}} \right)^{1/2} \times \left( \frac{kT_{\text{in}}}{1 \text{ keV}} \right)^{-2} M_{\odot} \quad (2)$$

(Soria 2007), where  $\eta$  is the radiative efficiency (in a semi-classical approximation,  $\eta \approx 1/12$  for a Schwarzschild BH, and  $\eta \approx 1/2$  for a maximally spinning Kerr BH),  $\kappa$  is a spectral hardening factor (ratio between colour temperature and effective temperature: Shimura & Takahara 1995),  $\xi$  is a normalization factor introduced because the peak tempera-

**Table 5.** Best-fitting parameters and F-test significance of additional spectral features (phenomenologically modelled as thermal-plasma emission or absorption edges) at all epochs in which they significantly improve the fit. Errors are 90% confidence limits for single parameters.

Epoch	Thermal Plasma			Edge		
	$kT$ (keV)	Normalization	Significance	$E$ (keV)	$\tau_{\max}$	Significance
2000 Mar 26 (H)	$0.61^{+0.06}_{-0.06}$	$(1.7^{+1.0}_{-1.1}) \times 10^{-5}$	> 99.9%			
	$0.98^{+0.16}_{-0.17}$	$(3.9^{+1.4}_{-1.4}) \times 10^{-5}$	> 95%			
	$2.5^{+*}_{-1.2}$	$(1.9^{+1.9}_{-1.6}) \times 10^{-5}$	> 95% <sup>1</sup>			
2000 Mar 26 (M)	$0.61^{+0.06}_{-0.06}$	$(2.6^{+0.5}_{-0.4}) \times 10^{-5}$	> 99%	$1.07^{+0.03}_{-0.03}$	$2.1^{+1.3}_{-0.8}$	> 99.9%
2004 Jul 5–11	$0.59^{+0.21}_{-0.26}$	$(2.9^{+4.6}_{-1.5}) \times 10^{-6}$	> 99%	$0.93^{+0.05}_{-0.04}$	$2.1^{+1.6}_{-0.9}$	> 99%
2005 Jan 1	$0.70^{+0.17}_{-0.13}$	$(3.1^{+1.5}_{-1.5}) \times 10^{-5}$	> 95%			
	$1.30^{+0.20}_{-0.20}$	$(4.3^{+1.7}_{-1.6}) \times 10^{-5}$	> 99%			

<sup>1</sup> This thermal plasma component is statistically equivalent to a *bremssstrahlung* or *comptt* component.

ture occurs outside the apparent inner radius (Kubota et al. 1998). For the M 101 ULS, the disk-blackbody temperatures and luminosities of the thermal component (Table 4) would require a BH mass of a few times  $10^3 M_{\odot}$  accreting at  $\sim 1\%$  of its Eddington limit. This is inconsistent with the results of Liu et al. (2013). Moreover, it is not self-consistent even within an IMBH scenario, because we do not expect an accreting BH to be in the high/soft state at such low Eddington ratios (see Equation 1), without a harder power-law component.

Finally, it is clear that the fitted value of  $R_{\text{in}}$  in the various observations is not consistent with being constant (Table 3), as should be for a disk in the high/soft state. This is equivalent to saying that there is also no  $L_{\text{diskbb}}^{\text{bol}} \propto T_{\text{in}}^4$  trend in the fitted distribution of temperatures and luminosities. There is instead an anticorrelation  $R \propto T^{-2}$  between fitted radius and temperatures (either in the blackbody or disk-blackbody model), which is more consistent with an expanding or contracting photosphere.

We are aware that none of those arguments is conclusive on its own. There are BHs in the high/soft state BHs that do not follow the  $L_{\text{diskbb}}^{\text{bol}} \propto T_{\text{in}}^4$  relation (*e.g.*, LMC X-1: Gierliński & Done 2004). This may be due to changes in the disk atmosphere, causing changes in the hardening factor (Salvesen et al. 2013; Reynolds & Miller 2013; Walton et al. 2013), instead of changes in the innermost radius of the disk. Nonetheless, when taken together, the lack of a standard disk track, the low luminosity for a high/soft state, and the high short-term variability make the standard disk interpretation very problematic for the M101 ULS. It was also shown (Urquhart & Soria 2015) that this source is not a lone exception: several other ULSs share similar properties, suggesting that the standard disk interpretation is not viable for the whole ULS class.

## 5.2 The outflow photosphere model

Given the serious problems of the standard disk interpretation (both in the stellar-mass and IMBH scenarios), we now examine the alternative possibility that the thermal emis-

sion in ULX-1 and other supersoft ULXs comes from the photosphere of a radiatively-driven outflow launched from an accretion disk in the super-Eddington accretion regime. Here, we follow and then extend the analysis of Shen et al. (2015), and we refer the readers to that paper for more detailed discussion of the outflow parameters.

Shen et al. (2015) define and solve a system of five equations for the outflow. Firstly, an equation for the absorption opacity  $\kappa_{\nu}^a$ :

$$\kappa_{\nu}^a = C \rho T^{-7/2} \text{ cm}^2 \text{ g}^{-1} \quad (3)$$

where  $\rho$  is the outflow gas density and  $C \approx 2.4 \times 10^{25}$ . The Thomson electron scattering opacity is  $\kappa_s \approx 0.2(1+X) \text{ cm}^{-2} \text{ g}^{-1}$ , where  $X$  is the hydrogen mass fraction. Henceforth, we assume that scattering dominates over absorption (as is the case in the inner part of accretion flows onto stellar-mass BHs), so that  $\kappa_s \gg \kappa_{\nu}^a$ . The second equation defines the thermalization radius  $R_{\text{th}}$  where the *effective* absorption optical depth  $\tau_{\nu}^* \equiv 1$ :

$$\tau_{\nu}^*(R_{\text{th}}) = \int_{R_{\text{th}}}^{\infty} \rho \sqrt{\kappa_{\nu}^a (\kappa_{\nu}^a + \kappa_s)} dr \approx \int_{R_{\text{th}}}^{\infty} \rho \sqrt{\kappa_{\nu}^a \kappa_s} dr = 1. \quad (4)$$

We are assuming that the outflow is accelerating (driven by radiation pressure) before reaching a constant speed: therefore, the outflow density drops at least as fast as  $r^{-2}$ . This simplifies the integration in Equation (4) and gives (Shen et al. 2015):

$$\rho(R_{\text{th}}) R_{\text{th}} \sqrt{\kappa_{\nu}^a \kappa_s} \approx 1. \quad (5)$$

Inside the thermalization radius, photons are in thermal equilibrium with the gas; beyond  $R_{\text{th}}$ , they are decoupled, in the sense that they are no longer absorbed and re-emitted (they can still scatter multiple times). Another characteristic radius of the outflow is the photon trapping radius  $R_{\text{tr}}$ : inside  $R_{\text{tr}}$ , photons are advected with the flow (diffusion timescale longer than the expansion timescale). As discussed by Shen et al. (2015), if the gas outflow is such that  $R_{\text{th}} > R_{\text{tr}}$ , the colour temperature of the photon spectrum observed at infinity is the temperature at the thermalization radius:  $T_{\text{th}} \equiv T(R_{\text{th}}) = T_{\text{bb}}$  (Shen et al. 2015). If  $R_{\text{th}} < R_{\text{tr}}$ ,

instead, the observed temperature  $T_{\text{bb}} = T(R_{\text{tr}})$ . Here, we follow the derivation for the case of the thermalization radius larger than the trapping radius: we will check later that this is indeed the case for the range of parameters suitable to the M101 ULS.

The third equation in the system of Shen et al. (2015) is the luminosity density from the radiative diffusion equation, which can be integrated over all photon energies to give:

$$L \approx \frac{16}{3} \pi R_{\text{th}}^2 \frac{\sigma T_{\text{th}}^4}{\tau_{\nu}(R_{\text{th}})}, \quad (6)$$

where  $\tau_{\nu}(R_{\text{th}})$  is the *total* optical depth (in our case, dominated by scattering), that is

$$\tau_{\nu}(R_{\text{th}}) = \int_{R_{\text{th}}}^{\infty} \rho(\kappa_{\nu}^a + \kappa_s) dr \approx \rho(R_{\text{th}}) \kappa_s R_{\text{th}} = \tau_s(R_{\text{th}}). \quad (7)$$

Finally, the fitted blackbody radius of the emerging radiation is *defined* as

$$R_{\text{bb}} \equiv \left( \frac{L}{4\pi\sigma T_{\text{bb}}^4} \right)^{1/2} \quad (8)$$

(notice that  $R_{\text{bb}} \neq R_{\text{th}}$  even in the approximation that  $T_{\text{bb}} = T_{\text{th}}$ ). By solving the system of equations (3), (5), (6), (7) and (8), Shen et al. (2015) determine the values of  $R_{\text{th}}$ ,  $\rho(R_{\text{th}})$  and  $\tau_s(R_{\text{th}})$  as a function of the observable quantities  $R_{\text{bb}}$ ,  $T_{\text{bb}}$  and  $L$ .

We want to go a step further, and express  $R_{\text{bb}}$ ,  $T_{\text{bb}}$  and  $L$  as a function of BH mass  $M \equiv mM_{\odot}$  and mass accretion rate  $\dot{M}$  at infinity,

$$\dot{M} \equiv \dot{m} \dot{M}_{\text{Edd}} \approx \frac{2.5 \times 10^{39}}{(1+X)c^2} m \dot{m} \text{ g s}^{-1}, \quad (9)$$

where we have defined the Eddington luminosity

$$L_{\text{Edd}} \equiv 0.1 \dot{M}_{\text{Edd}} c^2 \approx \frac{2.5 \times 10^{38}}{(1+X)} m \text{ erg s}^{-1} \quad (10)$$

for a hydrogen mass fraction  $X$ . Note that Shen et al. (2015) take  $L_{\text{Edd}} \approx 2 \times 10^{38} m \text{ erg s}^{-1}$  because they assume a Wolf-Rayet donor star (following Liu et al. (2013)) and therefore hydrogen-poor accretion flow; for the same reason, they take  $\kappa_s \approx 0.2 \text{ cm}^{-2} \text{ g}^{-1}$ . For our purpose, we need to introduce two additional equations that express for example  $\rho(R_{\text{th}})$  and  $L$  as a function of  $m$ ,  $\dot{m}$ . This was elegantly done in the outflow model of Poutanen et al. (2007), and we shall follow their lead (see also similar treatments in Strubbe & Quataert 2009; Lodato & Rossi 2011).

Let us start from the luminosity. The power output  $L_0$  of an outflow-dominated, super-Eddington accreting disk is  $L_0 = L_{\text{Edd}} \left(1 + \frac{3}{5} \ln \dot{m}\right)$ . However, a fraction  $\epsilon_w$  of that power is spent to accelerate the outflow; only a fraction  $(1 - \epsilon_w)$  emerges as radiative luminosity. Hence, the observed bolometric luminosity  $L$  is:

$$L = (1 - \epsilon_w) L_{\text{Edd}} \left(1 + \frac{3}{5} \ln \dot{m}\right) \quad (11)$$

with  $\epsilon_w \sim 0.5$  (Lipunova 1999; Poutanen et al. 2007). The amount of power used for accelerating the outflow depends of course on the mass loss rate in the outflow. That is a fraction  $f_{\text{out}}$  of the mass accretion rate at infinity:  $\dot{M}_w \equiv f_{\text{out}} \dot{M}$ . The kinetic fraction  $\epsilon_w$  is related to the mass outflow fraction  $f_{\text{out}}$  by the useful approximation  $f_{\text{out}} \approx 0.83\epsilon_w - 0.25\epsilon_w^2$

(Poutanen et al. 2007). For example,  $f_{\text{out}} = 0.5$  corresponds to  $\epsilon_w \approx 0.79$ .

Our second additional equation relates the outflow density to the accretion rate: for the conservation of mass,

$$\rho(R_{\text{th}}) = \frac{\dot{M}_w}{4\pi R_{\text{th}}^2 v_w} = \left( \frac{f_{\text{out}}}{f_v} \right) \frac{\dot{M}}{4\pi R_{\text{th}}^2 v_{\text{esc}}}, \quad (12)$$

where we have plausibly assumed that the outflow speed near the photosphere is of order of the escape velocity at the launching radius, that is  $v_w \equiv f_v v_{\text{esc}}$ . For the outflow launching radius, we assume that most of the wind comes from around the spherization radius  $R_{\text{sp}} \propto \dot{m}$  (King & Pounds 2003; Shakura & Sunyaev 1973). Poutanen et al. (2007) show that

$$R_{\text{sp}}/R_{\text{in}} \approx [1.34 - 0.4\epsilon_w + 0.1\epsilon_w^2] \dot{m} - (1.1 - 0.7\epsilon_w) \dot{m}^{1/3}. \quad (13)$$

Considering the uncertainty of the observed quantities and the other approximations of the model, we avoid unnecessary complications and take

$$R_{\text{sp}} \approx 1.1 \dot{m} R_{\text{in}} \quad (14)$$

where  $R_{\text{in}} = (6GM/c^2)$  for a non-rotating BH. Then,

$$v_{\text{esc}} = \left( \frac{2GM}{R_{\text{sp}}} \right)^{1/2} \approx 0.55 \frac{c}{\sqrt{\dot{m}}}. \quad (15)$$

Substituting Equations (9) and (15) into Equation (12):

$$\begin{aligned} \rho(R_{\text{th}}) &= \left( \frac{0.83\epsilon_w - 0.25\epsilon_w^2}{f_v} \right) \frac{\dot{M}}{4\pi R_{\text{th}}^2} \frac{\sqrt{\dot{m}}}{0.55c} \\ &= \left( \frac{0.83\epsilon_w - 0.25\epsilon_w^2}{f_v} \right) \frac{4.6 \times 10^{39}}{(1+X)c^3} \frac{m \dot{m}^{3/2}}{4\pi R_{\text{th}}^2}. \end{aligned} \quad (16)$$

Equations (11) and (16), added to the set of equations in Shen et al. (2015), allow us to model the observed temperature and luminosity as a function of BH mass and accretion rate.

From Equations (6), (7) and (8),

$$R_{\text{th}} = \sqrt{\frac{3}{4}} \sqrt{\tau_s} R_{\text{bb}}, \quad (17)$$

$$\rho(R_{\text{th}}) = \frac{\sqrt{\tau_s}}{\sqrt{(3/4) \kappa_s R_{\text{bb}}}}. \quad (18)$$

Substituting Equations (3), (6), (8), (17) and (18) into Equation (5):

$$\tau_s(R_{\text{th}}) = \left( \frac{3T_{\text{bb}} L \kappa_s^4}{16\pi\sigma C^2} \right)^{1/5}. \quad (19)$$

Moreover, from Equations (16) and (17):

$$\rho(R_{\text{th}}) = \left( \frac{0.83\epsilon_w - 0.25\epsilon_w^2}{f_v} \right) \frac{6.1 \times 10^{39}}{(1+X)c^3} \frac{m \dot{m}^{3/2}}{4\pi \tau_s R_{\text{bb}}^2}. \quad (20)$$

Dividing Equation (20) by Equation (18):

$$R_{\text{bb}} = 3.60 \times 10^6 \left( \frac{0.83\epsilon_w - 0.25\epsilon_w^2}{f_v} \right) \tau_s^{-3/2} m \dot{m}^{3/2} \text{ cm}, \quad (21)$$

and from Equations (8) and (11):

$$\begin{aligned} T_{\text{bb}} &= \frac{1.28 \times 10^7}{(1+X)^{1/4}} \frac{f_v^{1/2} (1 - \epsilon_w)^{1/4}}{(0.83\epsilon_w - 0.25\epsilon_w^2)^{1/2}} \tau_s^{3/4} \\ &\times m^{-1/4} \dot{m}^{-3/4} \left(1 + \frac{3}{5} \ln \dot{m}\right)^{1/4} \text{ K}. \end{aligned} \quad (22)$$

We solve for the scattering optical depth  $\tau_s(m, \dot{m})$  by inserting Equations (11) and (22) into (19):

$$\begin{aligned} \tau_s(R_{\text{th}}) &= 2189 \left( \frac{0.83\epsilon_w - 0.25\epsilon_w^2}{f_v} \right)^{-6/11} (1 - \epsilon_w)^{7/11} \\ &\times (1 + X)^{9/11} m^{1/11} \dot{m}^{-9/11} \\ &\times \left( 1 + \frac{3}{5} \ln \dot{m} \right)^{7/11}. \end{aligned} \quad (23)$$

Finally, we re-insert  $\tau_s(m, \dot{m})$  into Equations (21) and (22). After long but straightforward algebra, we obtain our final equations for the observed blackbody radius and temperature as a function of BH mass and accretion rate:

$$\begin{aligned} R_{\text{bb}} &= 35.2 \left( \frac{0.83\epsilon_w - 0.25\epsilon_w^2}{f_v} \right)^{20/11} (1 - \epsilon_w)^{-21/22} \\ &\times (1 + X)^{-27/22} m^{19/22} \dot{m}^{30/11} \\ &\times \left( 1 + \frac{3}{5} \ln \dot{m} \right)^{-21/22} \text{ cm}, \end{aligned} \quad (24)$$

$$\begin{aligned} T_{\text{bb}} &= 4.10 \times 10^9 \left( \frac{f_v}{0.83\epsilon_w - 0.25\epsilon_w^2} \right)^{10/11} (1 - \epsilon_w)^{8/11} \\ &\times (1 + X)^{4/11} m^{-2/11} \dot{m}^{-15/11} \\ &\times \left( 1 + \frac{3}{5} \ln \dot{m} \right)^{8/11} \text{ K}, \end{aligned} \quad (25)$$

approximately scaling as  $R_{\text{bb}} \propto T_{\text{bb}}^{-2}$  as expected.

### 5.3 Comparing the outflow model with the data

We now check whether our outflow photosphere model *can* produce blackbody temperatures, radii and luminosities consistent with the observed values (Table 3), for reasonable choices of parameters. We assume  $f_v = 1$ ,  $f_{\text{out}} = 0.5$  (*i.e.*, half of the accretion inflow is re-ejected in the wind before reaching the BH),  $X = 0$ , and a range of BH masses between  $5M_\odot$  and  $20M_\odot$ . We find that for  $\dot{m} \approx 400\text{--}700$ , the model does indeed predict colour temperatures  $\sim 50\text{--}130$  eV and characteristic radii  $\sim 10,000\text{--}100,000$  km, for BH masses  $\approx 10\text{--}20M_\odot$  (Figure 9, top left). Moreover, the bolometric luminosity predicted for the same range of BH masses is  $L_{\text{bb}}^{\text{bol}} \approx 2\text{--}5 \times 10^{39}$  erg s $^{-1}$  (Figure 9, top right), almost independent of accretion rate (and therefore of temperature and radius), in agreement with the observations. (Note again the absence of any  $L \propto T^4$  trend in the observational data.) Different choices of parameters within a plausible range can produce other model runs in agreement with the data: for example, for  $X = 0.73$  (solar abundance) and  $\epsilon_w = 0.5$  (corresponding to  $f_{\text{out}} \approx 1/3$ ), the fitted radii, temperatures and luminosities are obtained for BH masses  $\approx 10M_\odot$  and accretion rates  $\dot{m} \approx 900\text{--}1600$  (Figure 9, bottom panels).

We can also verify a posteriori that we were justified in assuming  $R_{\text{th}} > R_{\text{tr}}$ . For this condition to occur, the outflow velocity has to be smaller than a critical trapping speed (Shen et al. 2015):

$$v_w \approx 0.55 f_v \frac{c}{\sqrt{\dot{m}}} < v_{\text{crit}} \equiv \frac{c}{\tau_\nu} \approx \frac{c}{\tau_s}. \quad (26)$$

For  $X = 0$  and  $f_{\text{out}} = 0.5$ , we showed that the observational data suggests  $\dot{m} \approx 400\text{--}700$ . The characteristic outflow speed is  $v_w \approx 6000\text{--}8000$  km s $^{-1}$ , while  $\tau_s \approx 20\text{--}30$

(from Equation 23), and therefore  $v_{\text{crit}} \approx 10000\text{--}15000$  km s $^{-1}$ . For  $X = 0$  and  $f_{\text{out}} \approx 1/3$ ,  $\dot{m} \approx 1200\text{--}1600$ , implying a characteristic outflow speed  $v_w \approx 4000\text{--}6000$  km s $^{-1}$ . In this case,  $\tau_s \approx 30\text{--}40$ , and therefore  $v_{\text{crit}} \approx 7500\text{--}10000$  km s $^{-1}$ .

The kinetic power of the outflow at large distances can be estimated as follows. Let us assume (as representative values) an asymptotic outflow speed  $v_w \approx 7000$  km s $^{-1}$ ,  $\dot{m} \approx 500$ , and because  $f_{\text{out}} = 0.5$ ,  $\dot{m}_w \approx 250$ . For a  $10M_\odot$  BH, this corresponds to an outflow rate  $\dot{M}_w \approx 4 \times 10^{21}$  g s $^{-1}$ , and a kinetic power  $\approx 10^{39}$  erg s $^{-1}$ . The photon luminosity emitted at the base of the outflow is  $L = L_{\text{Edd}}[1 + (3/5) \ln \dot{m}] \approx 10^{40}$  erg s $^{-1}$  (larger than the photon luminosity at the photosphere by a factor  $1/(1 - \epsilon_w)$ ). A mechanical power in the fast wind  $P_w \approx 10\%$  of the (initial) photon luminosity is similar to what has been observed in fast-accreting AGN (*e.g.*, Tombesi et al. 2015) and predicted in MDH simulations of super-Eddington accretion (*e.g.*, Jiang et al. 2014). It is interesting to note that the most luminous standard ULXs within distances  $\lesssim 10$  Mpc reach X-ray luminosities of a few  $\times 10^{40}$  erg s $^{-1}$  (Swartz et al. 2004; Walton et al. 2011; Swartz et al. 2011), while the M101 ULS (and other ULXs: Urquhart & Soria 2015) reach luminosities of only a few  $\times 10^{39}$  erg s $^{-1}$ . We speculate that the upper envelope of total power output in ULXs corresponds to the upper envelope of luminosities in standard ULXs, after accounting for the reprocessing of a larger fraction of X-ray photons in the thicker outflow.

Another self-consistency check is required before we can use this outflow model. The thermalization radius must be larger than the launching radius (Equations 17 and 14, respectively). (Note that the physical thermalization radius is  $\approx 4\text{--}5$  times larger than the ‘‘apparent’’ blackbody radius derived from spectral fitting; see Equation 17). Substituting into the solution for  $R_{\text{th}}$ , this requires:

$$\begin{aligned} \frac{R_{\text{th}}}{R_{\text{sp}}} &= 1.5 \times 10^{-3} \left( \frac{0.83\epsilon_w - 0.25\epsilon_w^2}{f_v} \right)^{17/11} (1 + X)^{9/11} \\ &\times (1 - \epsilon_w)^{-7/11} m^{-1/11} \dot{m}^{29/22} \\ &\times \left( 1 + \frac{3}{5} \ln \dot{m} \right)^{-7/11} > 1. \end{aligned} \quad (27)$$

For the first set of parameters discussed above ( $X = 0$  and  $f_{\text{out}} = 0.5$ ), this condition is satisfied for  $\dot{m} \gtrsim 380$ . For the alternative set of parameters (solar abundance and  $f_{\text{out}} \approx 1/3$ ), it is satisfied only for  $\dot{m} \gtrsim 1250$ . However, our calculations were done assuming a spherically symmetric outflow and a Schwarzschild BH in the definition of spherization and launching radius. In practice, the outflow will be thicker closer to the equatorial plane; therefore a lower  $\dot{m}$  will be required to create an optically thick photosphere viewed from high inclination angles. As for the effect of BH spin, it is straightforward to solve the equations again for  $R_{\text{in}} = \alpha GM/c^2$  with  $1 < \alpha < 6$ , and verify that for fixed  $\dot{m}$  and decreasing  $\alpha$ ,  $R_{\text{th}}/R_{\text{sp}}$  scales approximately as  $1/\sqrt{\alpha}$ , and condition (27) is easier to satisfy.

The general physical significance of this model is that for any given line of sight, as the mass inflow rate and, as a result, also the outflow rate increase, at some point the wind will become effectively optically thick (as opposed to just optically thick to scattering) and will develop a thermalization surface. When that happens, the inner region of the inflow

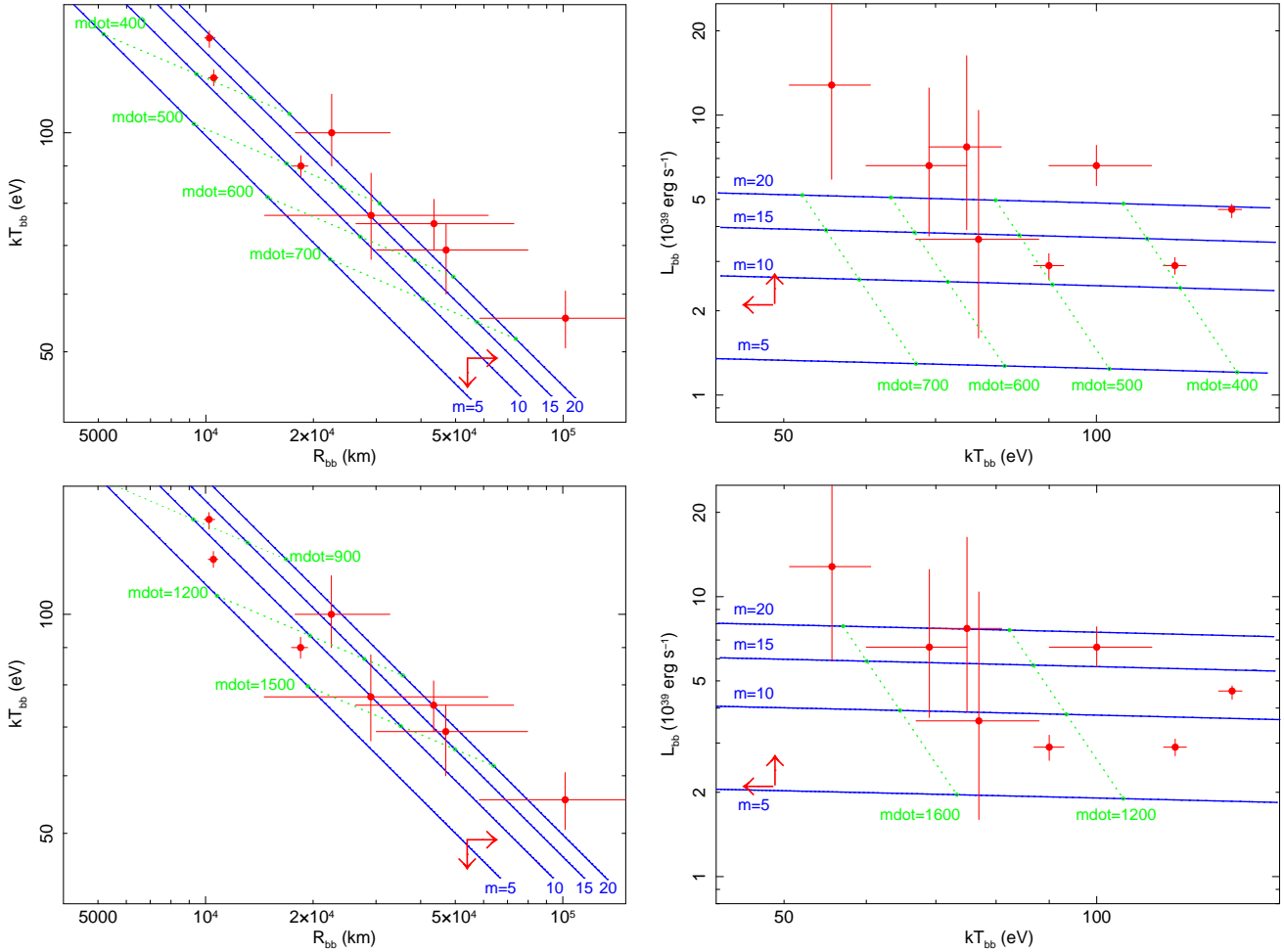


**Figure 9.** Predicted physical parameters from our super-Eddington outflow model, compared with the observations. Each solid blue curve represents the predicted values for a fixed BH mass (labelled next to each curve) over a range of accretion rates  $\dot{m}$ . Representative values of the accretion rates along each curve are also plotted (dotted green curves). The fitted datapoints from the *Chandra* observations are plotted in red (blackbody model; Table 3). Top left: colour temperature versus blackbody radius, assuming hydrogen-poor accretion ( $X = 0$ ),  $\epsilon_w = 0.79$ ,  $f_v = 1$ . Top right: bolometric luminosity versus colour temperature, for  $X = 0$ ,  $\epsilon_w = 0.79$ ,  $f_v = 1$ . Bottom left: colour temperature versus blackbody radius, assuming solar abundance ( $X = 0.73$ ),  $\epsilon_w = 0.5$ ,  $f_v = 1$ . Bottom right: bolometric luminosity versus colour temperature, for  $X = 0.73$ ,  $\epsilon_w = 0.5$ ,  $f_v = 1$ .

is shrouded by a photosphere (effective optical depth  $> 1$ ) which completely blocks our view of the inner disk/corona structure and makes the system look like a simple blackbody emitter with no high-energy tail. We used a spherical approximation for the wind in our model. We are aware that in reality, the outflow cannot be spherical, because it is launched from the accretion disk (among other reasons): for a fixed  $\dot{m}$ , the thickness of the wind will be higher for high-inclination line-of-sights, and lower when a source is seen more face-on, or even down the polar funnel, where the outflow is very tenuous and radiation escapes freely. Conversely, the higher the inclination, the lower the value of  $\dot{m}$  required to make the wind effectively optically thick. Nonetheless, we believe that a simple spherical approximation is useful to highlight the physical concept (in the same sense that a spherical approximation is used to define the Eddington accretion rate), and to estimate at least a characteristic order of magnitude for the accretion rate at which the wind at intermediate viewing angles is likely to become effectively op-

tically thick. Besides, for accretion rates as high as those discussed here ( $\dot{m} \sim$  a few 100), the polar funnel is predicted to be quite narrow and the outflow is likely to cover most of the  $4\pi$  solid angle around the BH. For example, it was proposed by King (2009) that the half-opening-angle  $\theta$  of the polar outflow scales as  $\theta \sim (150/\dot{m}^2)^{0.5}$ . The viewing-angle dependence on a ULX appearance was already extensively discussed in Sutton et al. (2013) and Middleton et al. (2015). The spectra of ObsID 934-high and ObsID 4737 might be a transitional stage between the supersoft regime and the standard ULX regime (soft thermal component plus high-energy tail carrying most of the flux), as the photospheric radius seen along our line of sight shrinks to the point where we start getting a direct view of harder photons emitted closer to the BH. Photospheric temperatures  $kT \approx 0.13$  keV may be the threshold between the two regimes.

#### 5.4 Donor star and binary period

An important feature of our spectral fits, reproduced by the outflow model, is that the bolometric luminosity is  $\gtrsim 10^{39}$  erg s $^{-1}$  even in the X-ray faint states. If accretion is radiatively efficient, this requires a long-term-average accretion rate  $\sim$  a few  $10^{-7} M_{\odot}$  yr $^{-1}$ , which is probably already too high to be consistent with wind accretion, advocated by the Liu et al. (2013) model. In fact, in our photosphere model, accretion is highly super-Eddington ( $\dot{m} \sim$  a few 100) and therefore less efficient. If the radiative efficiency of super-Eddington accretion flows scales as  $\eta \sim 0.1 (1 + \ln \dot{m})/\dot{m}$ , the required mass accretion rate at infinity is  $\approx 3 \times 10^{-4} M_{\odot}$  yr $^{-1}$ . The BH SS 433 is the only system in our Galaxy known so far that reaches such huge accretion rates (King & Begelman 1999; Fabrika 2004; Begelman et al. 2006; King 2009). Such mass transfer rates can occur over the thermal timescale or nuclear timescale of massive donor stars in their late stages of evolution (Rappaport et al. 2005). In particular, Wiktorowicz et al. (2015) showed that a  $10 M_{\odot}$  BH can be fed by a massive donor ( $M_2 \approx 10 M_{\odot}$ ) in the short-lived Hertzsprung gap phase, reaching a Roche-lobe overflow rate of  $\sim 10^{-3} M_{\odot}$  yr $^{-1}$  ( $\dot{m} \sim 1000$ ).

Crucially, such high accretion rates require that the donor star fills its Roche lobe. This is not the case for the orbital parameters measured by Liu et al. (2013). If their claimed orbital period of  $\approx (8.2 \pm 0.1)$  days (based on radial velocity measurements of the He II  $\lambda 4686$  emission line) is confirmed by future observations, our super-Eddington outflow model is all but ruled out. Conversely, we suggest that the empirical measurement of the orbital period may be incorrect, and the true period may be  $\lesssim 3$  days, so that the donor star does fill its Roche lobe.

One reason why we are not entirely convinced about the value of the period claimed by Liu et al. (2013) is that the He II emission was assumed to originate mainly from the Wolf-Rayet secondary with little contribution from the accretion disk. However, we do not know whether, or how much, the observed emission line is contaminated by emission from the hot gas inside the BH Roche lobe (outer disk, outflow, accretion stream, hot spot). Multiple variable contributions to He II emission are seen in other ULXs (Motch et al. 2014), and have prevented dynamical mass measurements (Roberts et al. 2011). Rapid, stochastic changes in the outflow density and temperature can easily change the X-ray luminosity (as shown by the rapid variability in the *Chandra* observations) and the irradiating flux, and hence change the relative contribution of different He II components. Another reason why we need to be cautious about the period measurement is that the sampling of radial velocities presented by Liu et al. (2013) is very sparse and does not even include a complete cycle. Two unrelated velocity dips around day 0 and day 90 (Fig. 2 in Liu et al. 2013), perhaps due to a contaminating component of He II, could explain the data equally well. With the current sampling, it is impossible to rule out periods smaller than 3 days (which would allow the donor star to fill its Roche lobe) or longer than 100 days.

#### 5.5 Contribution to the optical/UV emission

One of the main predictions of our model is that when a ULX is fainter in the soft X-ray band, it must be brighter

in the UV. The dimmest observations in which a thermal component is significantly detected show a characteristic blackbody temperature  $\approx 50$  eV ( $\approx 600,000$  K) and a characteristic radius  $\approx 100,000$  km. This is the case not just for this particular ULX in M 101, but also for most other ULXs (Urquhart & Soria 2015). At even lower temperatures, ULXs are simply impossible to detect with *Chandra* or *XMM-Newton*; however, in those cases, can the optically thick photosphere be directly detected in the UV band, for example with the *Hubble Space Telescope* (*HST*)? Assuming a reddening  $E(B - V) = 0.025$  (roughly corresponding to the line-of-sight  $N_{\text{H}} \approx 1.5 \times 10^{20}$  cm $^{-2}$ ),  $T_{\text{bb}} = 50$  eV,  $R_{\text{bb}} = 10^5$  km at the distance of M 101, the observed flux density at 2372.8 Å (effective wavelength of the F225W filter on *HST*'s Wide Field Camera 3) is  $F_{\nu} \approx 1.8 \times 10^{-8}$  Jy. This would result in a count rate of only  $\approx 0.02$  electrons s $^{-1}$ ; it would take an impossible 44,000 s to reach a signal-to-noise ratio of 7. The same blackbody spectrum gives a flux density  $F_{\nu} \approx 6 \times 10^{-9}$  Jy in the B band, corresponding to  $B \approx 29.6$  mag (again, currently undetectable). Besides, such low optical fluxes are swamped by the optical emission from the outer part of the accretion disk and the donor star; in the case of the M 101 ULX, the observed optical counterpart has a V-band flux density  $\approx 1.5 \times 10^{-6}$  Jy ( $V \approx 23.5$  mag; Liu 2009).

There is, however, a possibility that at some epochs the photosphere expands to even larger radii and the blackbody temperature becomes even cooler. At some point, the source may become detectable as an ultraluminous UV source. Such an object may have similarities with the compact, ultraluminous UV source (Kaaret et al. 2010) detected in the core of the ionized nebula MF16 (Dunne et al. 2000; Blair et al. 2001) in the galaxy NGC 6946. In that case, the emission from the powerful BH may have three components (Roberts et al. 2003; Abolmasov 2008; Kaaret et al. 2010): an ultraluminous X-ray component, a near-UV component with characteristic blackbody temperature  $\approx 23,000$ – $32,000$  K (consistent with the outer accretion disk and/or a massive donor star), and a far-UV source with characteristic temperature  $\approx 140,000$  K and characteristic radius  $\approx 2 \times 10^6$  km  $\approx 3 R_{\odot}$ . The far-UV component is not directly imaged but is inferred from the ionizing flux required to produce the observed He II  $\lambda 4686$  line emission from the optical nebula (Abolmasov 2008). There are not many astrophysical structures with the right size and temperature that can plausibly produce this far-UV component. It might be the optically thick photosphere of a large-scale outflow, even larger and cooler than what we modelled for the M 101 ULX; however, direct two-component X-ray emission is visible in the MF16 ULX (Roberts et al. 2003). The two scenarios are not in contradiction: the ULX may have been engulfed by a thick outflow a few decades ago, when the ionizing far-UV photons were emitted, and may now be in a lower accretion regime in which we see the X-ray emission from the inner accretion flow. Scaled to the distance of M 101, a hypothetical outflow photosphere with  $T_{\text{bb}} \approx 140,000$  K and  $R_{\text{bb}} \approx 2 \times 10^6$  km would have a flux density  $F_{\nu} \approx 1.6 \times 10^{-6}$  Jy in the F225W filter of *HST*/WFC3 (corresponding to  $\approx 2$  electrons s $^{-1}$ ); it would be seen in the optical band at  $B \approx 24.5$  mag,  $V \approx 25$  mag.

## 5.6 Absorption edges and harder emission tails

Even at the modest spectral resolution provided by *Chandra*/ACIS, we have confirmed the presence of absorption edges at  $E \approx 0.95\text{--}1.05$  keV, at some (but not all) epochs. The presence of (transient) edges was already noted as a ULS feature by Kong et al. (2004); see also Urquhart & Soria (2015) for further examples of ULSs with edges. Such absorption edges are not seen in two-component ULXs, which may be further evidence that ULSs are seen through thicker wind. The presence of absorption edges at various energies (in particular from OVIII) was predicted (but not yet observationally tested) for SS 433 as a key signature of super-critical outflows (Fabrika et al. 2006, 2007).

At some epochs, we found significant residuals (particularly around 0.7–2 keV) in addition to the dominant, super-soft blackbody component. Such residuals can be described as a hard excess, or a hard emission tail, with a luminosity of a few  $10^{38}$  erg s<sup>-1</sup> in the brightest epochs. We showed that multi-temperature, optically thin thermal plasma (*e.g.*, *mekal* in XSPEC) provides a good phenomenological fit to this harder emission. Similar spectral features around 1 keV, contributing a luminosity of a few  $10^{38}$  erg s<sup>-1</sup>, have been seen in some two-component ULXs (*e.g.*, NGC 5408 X-1 and NGC 6946 X-1) and have also been successfully fitted with thermal plasma emission (Middleton et al. 2014; Strohmayer et al. 2007; Stobbart et al. 2006). However, it was also argued (Middleton et al. 2014) that such features might instead be caused by broadened and blue-shifted absorption lines in a fast, partly ionized, optically-thin outflow. We do not have enough spectral resolution and signal-to-noise ratio to test between those two scenarios for the M 101 ULS. In either case, there is evidence both of an optically thick thermal emitter (which we argue is the photosphere of an optically thick outflow rather than the disk surface) and of a hotter component with absorption and/or emission features. Determining the origin of the hard tail and of the line features imprinted on it is beyond the scope of this work.

If all the excess hard emission comes from thermal-plasma components, we can use the model normalization to estimate the total amount of emitting gas visible to us. For ObsID 934-high, we have  $\int n_e n_H dV \approx 4 \times 10^{61}$  cm<sup>-3</sup>. Taking the fitted value  $R_{\text{bb}} \approx 10^9$  cm as a characteristic length scale for the emitting gas, so that  $V \approx 10^{27}$  cm<sup>3</sup>, we obtain  $n_e \approx 2 \times 10^{17}$  cm<sup>-3</sup>, that is  $\rho \approx 3 \times 10^{-7}$  g cm<sup>-3</sup> for ionized hydrogen gas. We obtain a similar back-of-the-envelope estimate for the emission from ObsID 4737. For ObsID 934-medium, the estimated amount of optically-thin gas is slightly lower,  $\rho \approx 10^{-7}$  g cm<sup>-3</sup>. This characteristic density compares well with the density range of the clumpy medium in the MHD simulations of Takeuchi et al. (2013) (see in particular their Fig. 1), at a comparable radial distance from the BH ( $\sqrt{R^2 + z^2} \sim 10^4$  km).

Hard X-ray emission (modelled with bremsstrahlung or thermal plasma) from optically thin plasma, in addition to the dominant blackbody-like supersoft component, is often found in classical novae (Orio et al. 1996; Balman et al. 1998; Sokoloski et al. 2006; Hernanz & Sala 2010; Li et al. 2012). It is generally explained with internal shocks in the expanding envelope, and/or shocks between the fast wind and circumstellar medium. One possible scenario applicable to the M 101 ULS, in which the donor star is a Wolf-Rayet, is

that some hard X-ray emission originates from interactions and shocks between the BH outflow and the Wolf-Rayet wind. This can perhaps explain the faint ( $L_{0.3-10} \approx 1 \times 10^{37}$  erg s<sup>-1</sup>) power-law component significantly detected only in the very deep, stacked spectrum of the dim-state observation but consistent with being present at all times. On the other hand, the much stronger hard X-ray component seen especially in ObsID 934 and ObsID 4737 varies on the same short timescales as the soft-band emission. This is difficult to explain if one component comes from stellar wind interactions at  $R \gtrsim 10^{11}$  cm and the other from much nearer the BH ( $R_{\text{bb}} \approx 10^9$  cm). Therefore, we suggest that the hard tail is emitted either from the same region as the optically thick blackbody (perhaps a clumpy outflow, with optically thick clouds in between a hotter, lower-density medium), or even from smaller radii.

## 6 CONCLUSIONS

The supersoft thermal spectrum of the M 101 ULS (as well as those of a few other ULSs) has sometimes been interpreted as disk emission. Here, we re-examined the X-ray spectral and timing data from a series of *Chandra* and *XMM-Newton* observations, and discussed the main problems and internal inconsistencies of that interpretation. Instead, we showed that a model based on the photosphere of an optically thick outflow is consistent with the empirical data. For example, we showed that for  $\dot{m} \approx 400\text{--}700$ , our phenomenological model predicts (for BH masses  $\approx 10M_{\odot}$ ) blackbody temperatures  $\sim 50\text{--}130$  eV, characteristic radii  $\sim 10,000\text{--}100,000$  km, and bolometric luminosities  $L_{\text{bb}}^{\text{bol}} \sim$  a few times  $10^{39}$  erg s<sup>-1</sup>, in agreement with the observations. In this scenario, the apparent brightness changes of the M 101 ULS are mostly due to fast changes in the effective photospheric radius within a clumpy, fast outflow. When the photosphere expands, its characteristic temperature moves out of the *Chandra* band and into the far-UV band. The accretion rate is always highly super-critical, and the apparent faint states would appear just as luminous if observed in the far-UV.

Assuming that the massive wind is launched from near the spherization radius, and using a simple spherical and uniform analytic approximation for the outflow, we have argued that there is a critical accretion rate ( $\dot{m} \sim$  a few 100, corresponding to  $\dot{M} \sim 10^{-4} M_{\odot}$  yr<sup>-1</sup> for a stellar-mass BH) above which the outflow becomes effectively optically thick and completely shrouds the harder emission from the inner part of the accretion flow ( $R < R_{\text{sp}}$ ). In a more realistic, non-spherically-symmetric model, the wind is thicker when seen at higher inclination, and the corresponding threshold in  $\dot{m}$  will have an angle dependence. We suggested that if the accretion rate drops below this limit, and the photosphere shrinks, we may see a harder tail re-emerge in the observed spectrum, with a slope and high-energy break depending on the scattering optical depth in the wind (Sutton et al. 2013).

The soft thermal component of standard two-component ULXs is typically  $\approx 130\text{--}300$  eV (Miller et al. 2004; Kajava & Poutanen 2009; Stobbart et al. 2006), and some authors have suggested (Soria 2007; Kajava & Poutanen 2009) that the temperature decreases with increasing accretion rate (but see Miller et al. 2013 for an opposite interpretation). On the other hand,

the typical blackbody temperature of ULXs is  $\approx 50\text{--}150$  eV. We suggest that  $T_{\text{bb}} \approx T_{\text{disk}}(R = R_{\text{sp}}) \approx 100\text{--}150$  eV is the critical threshold at which an outflow photosphere develops and shrouds the ULX: below those temperatures, hard energy tails are rarely seen, while they are usually observed in sources at higher temperatures. A comparison between the fitted temperature and luminosities of a larger sample of ULXs and ULXs is left to a companion paper (Urquhart & Soria 2015). In support of our suggested link between ULXs and ULXs, we noted that in the epochs when the fitted blackbody radius of the M101 ULX is larger, the temperature is lower and the spectrum is well modelled with a single blackbody component. In some of the epochs when the radius is smaller and the temperature higher, we found comparatively strong emission above 1.5 keV, which is consistent either with an additional, hotter thermal plasma component or with an inverse-Compton tail.

We also argued that the accretion rates required to produce a ULX in our scenario (especially if viewed at high inclination) are extremely high but not physically impossible: there is at least one source in our Galaxy (SS433) with a comparable accretion rate. Recent theoretical models of binary evolution (Wiktorowicz et al. 2015) support the existence of such systems, provided that the donor star is filling its Roche lobe. In the specific case of the M101 ULX, this requirement appears to be inconsistent with a claimed orbital period of  $\approx 8$  days (Liu et al. 2013). We argued that such optical variability measurement may not correspond to the true period, and further investigations on this issue are needed (but are beyond the scope of this paper).

## ACKNOWLEDGMENTS

We thank Ryan Urquhart, Hua Feng, Jan-Uwe Ness, Manfred Pakull, Christian Motch, Doug Swartz, Chris Done, Yan-Fei Jiang, Rosanne Di Stefano, James Miller-Jones, Tom Russell, Peter Curran for useful suggestions and discussions. We also thank the anonymous referee for many useful suggestions. RS acknowledges support from a Curtin University Senior Research Fellowship. He is also grateful for support and hospitality at Tsinghua University (Beijing) and Strasbourg Observatory during part of this work. This paper benefitted from discussions at the 2015 International Space Science Institute workshop ‘‘The extreme physics of Eddington and super-Eddington accretion onto Black Holes’’ in Bern, Switzerland (team PIs: Diego Altamirano & Omer Blaes).

## REFERENCES

Abolmasov P., Fabrika S., Sholukhova O., Kotani T., 2008, arXiv:0809.0409  
 Arnaud K.A., 1996, *Astronomical Data Analysis Software and Systems V* (ASP Conf. Ser. 101), ed. G.H. Jacoby & J. Barnes (San Francisco, CA: ASP), 17  
 Balman Ş., Krautter J., Ögelman H., 1998, *ApJ*, 499, 395  
 Begelman M.C., King A.R., Pringle J.E., 2006, *MNRAS*, 370, 399  
 Belczynski K., Bulik T., Fryer C.L., Ruiter A., Valsecchi F., Vink J.S., Hurley J.R., 2010, *ApJ*, 714, 1217

Belloni T.M., 2010, *LNP*, 794, 53  
 Blackburn J.K., 1995, *Astronomical Data Analysis Software and Systems IV* (ASP Conf. Ser. 77), ed. R.A. Shaw, H.E. Payne, & J.J.E. Hayes (San Francisco, CA: ASP), 367  
 Blair W.P., Fesen R.A., Schlegel E.M., 2001, *AJ*, 121, 1497  
 Carpano S., Wilms J., Schirmer M., Kendziorra E., 2006, *A&A*, 458, 747  
 Carpano S., Pollock A.M.T., King A.R., Wilms J., Ehle M., 2007, *A&A*, 471, L55  
 Davis J.E., 2001, *ApJ*, 562, 575  
 Di Stefano R., Kong A.K.H., 2003, *ApJ*, 592, 884  
 Di Stefano R., Kong A.K.H., 2004, *ApJ*, 609, 710  
 Done C., Davis S.W., Jin C., Blaes O., Ward M., 2012, *MNRAS*, 420, 1848  
 Dotan C., Shaviv N.J., 2011, *MNRAS*, 413, 1623  
 Dunne B.C., Gruendl R.A., Chu Y.-H., 2000, *AJ*, 119, 1172  
 Edelson R., Turner T.J., Pounds K., Vaughan S., Markowitz A., Marshall H., Dobbie P., Warwick R., 2002, *ApJ*, 568, 610  
 Fabbiano G., King A.R., Zezas A., Ponman T.J., Rots A., Schweizer F., 2003, *ApJ*, 591, 843  
 Fabrika S., 2004, *ASPRv*, 12, 1  
 Fabrika S.N., Karpov S., Abolmasov P.K., Sholukhova O., 2006, *IAUS*, 230, 278  
 Fabrika S.N., Abolmasov P.K., Karpov S. 2007, *IAUS*, 238, 225  
 Farrell S.A., Webb N.A., Barret D., Godet O., Rodrigues J.M. 2009, *Nature*, 460, 73  
 Fender R.P., Belloni T.M., Gallo E., 2004, *MNRAS*, 355, 1105  
 Feng H., Kaaret P., 2010, *ApJ*, 712, L169  
 Feng H., Soria R., 2011, *NewA Rev.*, 55, 166  
 Frank J., King A.R., Raine D.J., 2002, *Accretion Power in Astrophysics* (Cambridge: Cambridge University Press)  
 Freedman W.L., et al., 2001, *ApJ*, 553, 47  
 Fruscione A., et al., 2006, in *Society of Photo-Optical Instrumentation Engineers (SPIE) Conference Series*, 6270, 1  
 Gierliński M., Done C., 2004, *MNRAS*, 347, 885  
 Gierliński M., Zdziarski A.A., 2005, *MNRAS*, 363, 1349  
 Gladstone J.C., Roberts T.P., Done C., 2009, *MNRAS*, 397, 1836  
 Greiner J., 2000, *NewA*, 5, 137  
 Greiner J., Di Stefano R., Kong A.K.H., Primini F., 2004, *ApJ*, 610, 261  
 Hachisu I., Kato M., Nomoto K., 1996, *ApJ*, 470, L97  
 Hernanz M., Sala G., 2010, *AN*, 331, 169  
 Houck J.C., Denicola, L.A., 2000, *Astronomical Data Analysis Software and Systems IX* (ASP Conf. Ser. 216), ed. N. Manset, C. Veillet & D. Crabtree (San Francisco, CA: ASP), 591  
 Jenkins L.P., Roberts T.P., Warwick R.S., Kilgard R.E., Ward M.J., 2004, *MNRAS*, 349, 404  
 Jin J., Feng H., Kaaret P., Zhang S.-N., 2011, *ApJ*, 737, 87  
 Jiang Y.-F., Stone J.M., Davis S.W., 2014, *ApJ*, 796, 106  
 Kaaret P., Feng H., Wong D.S., Tao L., 2010, *ApJ*, 714, L167  
 Kahabka P., van den Heuvel E.P.J., 1997, *ARA&A*, 35, 69  
 Kajava J.J.E., Poutanen J., 2009, *MNRAS*, 398, 1450  
 Kawashima T., Ohsuga K., Mineshige S., Yoshida T., Heinzeller D., Matsumoto R., 2012, *ApJ*, 752, 18

- King A.R., 2009, MNRAS, 393, L41  
King A.R., Begelman M.C., 1999, ApJ, 519, L169  
King A.R., Pounds K.A., 2003, MNRAS, 345, 657  
Kong A.K.H., Di Stefano R., 2003, ApJ, 590, L13  
Kong A.K.H., Di Stefano R., 2005, ApJ, 632, L107  
Kong A.K.H., Di Stefano R., Yuan F., 2004, ApJ, 617, L49  
Kreidberg L., Bailyn C.D., Farr W.M., Kalogera V., 2012, ApJ, 757, 36  
Kubota A., Makishima K., 2004, ApJ, 601, 428  
Kubota A., Tanaka Y., Makishima K., Ueda Y., Dotani T., Inoue H., & Yamaoka K., 1998, PASJ, 50, 667  
Li K.L., et al., 2012, ApJ, 761, 99  
Lipunova G.V., 1999, AstL, 25, 508  
Liu J.-F., 2008, ApJS, 177, 181  
Liu J.-F., 2009, ApJ, 704, 1628  
Liu J.-F., Bregman J.N., Bai Y., Justham S., Crowther P., 2013, Nature, 503, 500  
Liu J.-F., Di Stefano R., 2008, ApJ, 674, L73  
Lodato G., Rossi E.M., 2011, MNRAS, 410, 350  
Maccarone T.J., 2003, A&A, 409, 697  
McClintock J.E., Remillard R.A., 2006, Black Hole Binaries, ed. W.H.G. Lewin & M. van der Klis (Cambridge: Cambridge Univ. Press), 157  
Makishima K., Maejima Y., Mitsuda K., Bradt H.V., Remillard R.A., Tuohy I.R., Hoshi R., Nakagawa M., 1986, ApJ, 308, 635  
Markowitz A., Edelson R., Vaughan S., 2003, ApJ, 598, 935  
Middleton M.J., Roberts T.P., Done C., Jackson F.E., 2011, MNRAS, 411, 644  
Middleton M.J., Walton D.J., Roberts T.P., Heil L., 2014, MNRAS, 438, L51  
Middleton M.J., Heil L., Pintore F., Walton D.J., Roberts T.P., 2015, MNRAS, 447, 3243  
Miller J.M., Fabian A.C., Miller M.C., 2004, ApJ, 614, L117  
Miller J.M., Walton D.J., King A.L., Reynolds M.T., Fabian A.C., Miller M.C., Reis R.C., 2013, ApJ, 776, L36  
Mizuno T., Kubota A., Makishima K., 2001, ApJ, 554, 1282  
Motch C., Pakull M.W., Soria R., Grisé F., Pietrzyński G., 2014, Nature, 514, 198  
Mukai K., Pence W.D., Snowden S.L., Kuntz K.D., 2003, ApJ, 582, 184  
Mukai K., Still M., Corbet R., Kuntz K.D., Barnard R., 2005, ApJ, 634, 1085  
Mukherjee E.S., et al., 2015, ApJ, 808, 64  
Ness J.-U., Schwarz G., Starrfield S., Osborne J.P., Page K.L., Beardmore A.P., Wagner R.M., Woodward C.E., 2008, AJ, 135, 1328  
Ness J.-U., et al., 2013, A&A, 559, 50  
Ohsuga K., Mineshige S., 2011, ApJ, 736, 2  
Orio M., Balman S., della Valle M., Gallagher J., Ögelman H., 1996, ApJ, 466, 410  
Orio M., Nelson T., Bianchini A., Di Mille F., Harbeck D., 2010, ApJ, 717, 7390  
Pakull M.W., Motch C., Bianchi L., Thomas H.-C., Guibert J., Beaulieu J.P., Grison P., Schaeidt S., 1993, A&A, 278, L39  
Pasham D.R., Strohmayer T.E., Mushotzky R.F., 2014, Nature, 513, 74  
Poutanen J., Lipunova G., Fabrika S., Butkevich A.G., Abolmasov P., 2007, MNRAS, 377, 1187  
Protassov R., van Dyk D.A., Connors A., Kashyap V.L., Siemiginowska A., 2002, ApJ, 571, 545  
Rappaport S.A., Di Stefano R., Smith J.D., 1994, ApJ, 426, 692  
Rappaport S.A., Podsiadlowski P., Pfahl E., 2005, MNRAS, 356, 401  
Read A.M., Pietsch W., 2001, A&A, 373, 473  
Reynolds M.T., Miller J.M., 2013, ApJ, 769, 16  
Roberts T.P., 2007, Ap&SS, 311, 203  
Roberts T.P., Colbert E.J.M., 2003, MNRAS, 341, L49  
Roberts T.P., Gladstone J.C., Goulding A.D., Swinbank A.M., Ward M.J., Goad M.R., Levan A.J., 2011, AN, 332, 398  
Salvesen G., Miller J.M., Reis R.C., Begelman M.C., 2013, MNRAS, 431, 3510  
Shakura N.I., Sunyaev R.A., 1973, A&A, 24, 337  
Shappee B.J., Stanek K.Z. 2011, ApJ, 733, 124  
Shen R.-F., Barniol Duran R., Nakar E., Piran T., 2015, MNRAS, 447, L60  
Shimura T., Takahara F., 1995, ApJ, 445, 780  
Skopal A., 2015a, NewA, 36, 128  
Skopal A., 2015b, NewA, 36, 139  
Sokoloski J.L., Luna G.J.M., Mukai K., Kenyon S.J., 2006, Nature, 442, 276  
Soria R., 2007, Ap&SS, 311, 213  
Soria R., Ghosh K.K., 2009, ApJ, 696, 287  
Steiner J.F., McClintock J.E., Remillard R.A., Narayan R., Gou L.J., ApJ, 701, L83  
Stobbart A.-M., Roberts T.P., Wilms J., 2006, MNRAS, 368, 397  
Strohmayer T.E., Mushotzky R.F., Winter L., Soria R., Uttley P., Cropper M., 2007, ApJ, 660, 580  
Strubbe L.E., Quataert E., 2009, MNRAS, 400, 2070  
Sutton A.D., Roberts T.P., Middleton M.J., 2013, MNRAS, 435, 1758  
Swartz D.A., Ghosh K.K., Suleimanov V., Tennant A.F., Wu K., 2002, ApJ, 574, 382  
Swartz D.A., Ghosh K.K., Tennant A.F., Wu K., 2004, ApJS, 154, 519  
Swartz D.A., Soria R., Tennant A.F., Yukita M., 2011, ApJ, 741, 49  
Takeuchi S., Ohsuga K., Mineshige S. 2013, PASJ, 65, 88  
Tao L., Feng H., Kaaret P., Grisé F., Jin J., 2012, ApJ, 758, 85  
Terashima Y., Wilson A.S., 2004, ApJ, 601, 735  
Tombesi F., Meléndez M., Veilleux S., Reeves J.N., González-Alfonso E., Reynolds C.S., 2015, Nature, 519, 436  
Urquhart R.T., Soria R., 2015, MNRAS, in press  
van den Heuvel E.P.J., Bhattacharya D., Nomoto K., Rappaport S.A., 1992, A&A, 262, 97  
Vaughan S., Edelson R., Warwick R.S., Uttley P., 2003, MNRAS, 345, 1271  
Vogler A., Pietsch W., 1996, A&A, 311, 35  
Walton D.J., Roberts T.P., Mateos S., Heard V. 2011, MNRAS, 416, 1844  
Walton D.J., et al., 2013, ApJ, 779, 148  
Walton D.J., et al., 2015, ApJ, 806, 65  
Wang Q.D., Immler S., Pietsch W., 1999, ApJ, 523, 121  
Watarai K., Mizuno T., Mineshige S., 2001, ApJ, 549, L77  
Wiktorowicz G., Sobolewska M., Sadowski A., Belczynski K., 2015, ApJ, 810, 20

**APPENDIX A: X-RAY SPECTRAL PARAMETERS**

In the following tables, we list the best-fitting spectral parameters for a selection of spectral models and epochs. More specifically, we show (Table A1) how the high-count-rate interval of ObsID 934 requires harder components in addition to the soft thermal emission (this confirms the results of Mukai et al. 2003 over the same time intervals). We then present (Table A2) a simultaneous fit of high-, intermediate- and low-count-rate intervals of ObsID 934, where we have fixed the intrinsic column density and the temperature of three thermal-plasma components, but we let their normalizations free; the temperature and normalization of the dominant blackbody component are also free. This model is illustrated in Figure 5. We then repeat the simultaneous fit to the same three intervals of ObsID 934 using two thermal-plasma components, accounting for the emission features at  $\sim 0.5$ –1 keV, and one Comptonization component, accounting for the hard excess above 1 keV (Table A3). We find that the model that includes the Comptonization component is statistically equivalent to the one that includes instead a high-temperature thermal plasma component. Finally, we list the best-fitting parameters for all other epochs: Table A4 is for the *Chandra* observations (plotted in Figures 3,4), and Table A5 for the *XMM-Newton* observation (Figure 8).

	Model 1	Model 2	Model 3	Model 4	Model 5
Parameter	Value				
$g_0$		[1]	[1]	[1]	[1]
$\alpha$		$0.36^{+0.07}_{-0.09}$	$0.34^{+0.08}_{-0.08}$	$0.25^{+0.08}_{-0.08}$	$0.21^{+0.09}_{-0.07}$
psfrac		[0.85]	[0.85]	[0.85]	[0.85]
$N_{\text{H,Gal}}$ ( $10^{20}$ cm $^{-2}$ )	[1.5]	[1.5]	[1.5]	[1.5]	[1.5]
$N_{\text{H,int}}$ ( $10^{20}$ cm $^{-2}$ )	< 0.8	$1.9^{+2.1}_{-1.8}$	$2.7^{+2.1}_{-1.7}$	$2.2^{+1.5}_{-0.8}$	$5.6^{+1.4}_{-0.7}$
$kT_{\text{bb}}$ (eV)	$178^{+3}_{-3}$	$159^{+9}_{-9}$	$140^{+9}_{-11}$	$138^{+6}_{-7}$	
$R_{\text{bb}}$ ( $10^3$ km)	$4.3^{+0.3}_{-0.2}$	$7.1^{+0.2}_{-0.9}$	$9.2^{+3.0}_{-1.2}$	$9.1^{+0.4}_{-0.4}$	
$kT_{\text{in}}$ (eV)					$174^{+6}_{-7}$
$r_{\text{in}}\sqrt{\cos\theta}$ ( $10^3$ km)					$5.9^{+0.3}_{-0.3}$
$kT_{\text{mekal1}}$ (keV)			$0.88^{+0.13}_{-0.10}$	$0.76^{+0.09}_{-0.09}$	$0.72^{+0.09}_{-0.09}$
$N_{\text{mekal1}}$			$4.8^{+1.5}_{-1.3} \times 10^{-5}$	$4.1^{+0.8}_{-0.8} \times 10^{-5}$	$4.8^{+0.8}_{-0.8} \times 10^{-5}$
$kT_{\text{mekal2}}$ (keV)				$1.6^{+1.3}_{-0.4}$	$1.7^{+1.2}_{-0.4}$
$N_{\text{mekal2}}$				$4.0^{+1.5}_{-1.5} \times 10^{-5}$	$4.0^{+1.5}_{-1.5} \times 10^{-5}$
$\chi^2_{\nu}$	2.23 (176.2/79)	1.65 (128.7/78)	1.23 (93.2/76)	1.15 (84.9/74)	1.16 (85.5/74)
$f_{0.3-10}$ ( $10^{-13}$ erg cm $^{-2}$ s $^{-1}$ )	$3.8^{+0.2}_{-0.2}$	$5.6^{+0.2}_{-0.2}$	$5.7^{+0.2}_{-0.2}$	$6.1^{+0.2}_{-0.2}$	$6.1^{+0.2}_{-0.2}$
$L_{0.3-10}$ ( $10^{39}$ erg s $^{-1}$ )	$2.0^{+0.1}_{-0.1}$	$3.4^{+0.2}_{-0.2}$	$3.8^{+0.2}_{-0.2}$	$3.9^{+0.2}_{-0.2}$	$5.2^{+0.3}_{-0.3}$
$L_{\text{bb}}^{\text{bol}}$ ( $10^{39}$ erg s $^{-1}$ )	$2.4^{+0.1}_{-0.1}$	$4.1^{+0.7}_{-0.5}$	$4.1^{+0.7}_{-0.2}$	$4.0^{+0.2}_{-0.1}$	
$L_{\text{d bb}}^{\text{bol}} \cos\theta$ ( $10^{39}$ erg s $^{-1}$ )					$4.1^{+0.2}_{-0.2}$

**Table A1.** Best-fitting spectral parameters for the high-count-rate intra-observation interval of *Chandra* ObsID 934, fitted with four different models. Model 1 is  $tbabs \times tbabs \times blackbody$ . Model 2 is  $pileup \times tbabs \times tbabs \times blackbody$ . Model 3 is  $pileup \times tbabs \times tbabs \times (mekal + mekal + blackbody)$ . Model 4 is  $pileup \times tbabs \times tbabs \times (mekal + mekal + diskbb)$ . The *mekal* normalization is in units of  $10^{-14}/(4\pi d^2) \int n_e n_H dV$ . Errors indicate the 90% confidence interval for each parameter of interest. See also Figure 3.

	Interval 1 (high)	Interval 2 (medium)	Interval 3 (low)
Parameter	Value		
$g_0$	[1]	[1]	[1]
$\alpha$	$0.27^{+0.08}_{-0.08}$	$0.34^{+0.09}_{-0.10}$	[0]
psffrac	[0.85]	[0.85]	[0.85]
$N_{\text{H,Gal}}$ ( $10^{20}$ cm $^{-2}$ )	[1.5]	[1.5]	[1.5]
$N_{\text{H,int}}$ ( $10^{20}$ cm $^{-2}$ )	$(4.1^{+0.4}_{-0.4})$	$(4.1^{+0.4}_{-0.4})$	$(4.1^{+0.4}_{-0.4})$
$kT_{\text{bb}}$ (eV)	$135^{+3}_{-4}$	$119^{+3}_{-3}$	$90^{+3}_{-3}$
$R_{\text{bb}}$ ( $10^3$ km)	$10.2^{+0.4}_{-0.3}$	$10.5^{+0.3}_{-0.3}$	$18.4^{+0.9}_{-1.0}$
$kT_{\text{edge}}$ (keV)	$(1.07^{+0.03}_{-0.05})$	$(1.07^{+0.03}_{-0.05})$	$(1.07^{+0.03}_{-0.05})$
$\tau_{\text{edge}}$	[0]	$2.1^{+1.3}_{-0.8}$	[0]
$kT_{\text{mekal1}}$ (keV)	$(0.61^{+0.06}_{-0.06})$	$(0.61^{+0.06}_{-0.06})$	$(0.61^{+0.06}_{-0.06})$
$N_{\text{mekal1}}$	$1.7^{+1.0}_{-1.1} \times 10^{-5}$	$2.3^{+0.5}_{-0.4} \times 10^{-5}$	[0]
$kT_{\text{mekal2}}$ (keV)	$(0.98^{+0.16}_{-0.17})$	$(0.98^{+0.16}_{-0.17})$	$(0.98^{+0.16}_{-0.17})$
$N_{\text{mekal2}}$	$3.9^{+1.4}_{-1.4} \times 10^{-5}$	$< 0.30 \times 10^{-5}$	[0]
$kT_{\text{mekal3}}$ (keV)	$(2.5^{+*}_{-1.2})$	$(2.5^{+*}_{-1.2})$	$(2.5^{+*}_{-1.2})$
$N_{\text{mekal3}}$	$1.9^{+1.9}_{-1.6} \times 10^{-5}$	$< 0.56 \times 10^{-5}$	[0]
$\chi^2_{\nu}$	(1.21 (174.6/144))	(1.21 (174.6/144))	(1.21 (174.6/144))
$f_{0.3-10}$ ( $10^{-13}$ erg cm $^{-2}$ s $^{-1}$ )	$5.9^{+0.2}_{-0.2}$	$2.9^{+0.2}_{-0.2}$	$1.6^{+0.3}_{-0.3}$
$L_{0.3-10}$ ( $10^{39}$ erg s $^{-1}$ )	$4.3^{+0.2}_{-0.2}$	$2.3^{+0.2}_{-0.2}$	$1.5^{+0.3}_{-0.3}$
$L_{\text{bb}}^{\text{bol}}$ ( $10^{39}$ erg s $^{-1}$ )	$4.6^{+0.2}_{-0.3}$	$2.9^{+0.2}_{-0.2}$	$2.9^{+0.3}_{-0.3}$

**Table A2.** Best-fitting spectral parameters for *Chandra* ObsID 934, fitted with  $\text{pileup} \times \text{tbabs} \times \text{tbabs} \times \text{edge} \times (\text{mekal} + \text{mekal} + \text{mekal} + \text{blackbody})$ . This was a simultaneous fit to the spectra in the three intra-observation intervals, defined from the observed count rates (high, medium, low). Parameters listed in square brackets were frozen during the fit; parameters listed in round brackets were free but locked for all three spectra; all other parameters were left free to vary independently. The *mekal* normalization is in units of  $10^{-14}/(4\pi d^2) \int n_e n_H dV$ . Errors indicate the 90% confidence interval for each parameter of interest. The fitted spectra and  $\chi^2$  residuals are plotted in Figure 2 (top left panel).

Parameter	Interval 1 (high)	Interval 2 (medium)	Interval 3 (low)
	Value		
$g_0$	[1]	[1]	[1]
$\alpha$	$0.27^{+0.09}_{-0.08}$	$0.34^{+0.09}_{-0.10}$	[0]
psffrac	[0.85]	[0.85]	[0.85]
$N_{\text{H,Gal}}$ ( $10^{20}$ cm $^{-2}$ )	[1.5]	[1.5]	[1.5]
$N_{\text{H,int}}$ ( $10^{20}$ cm $^{-2}$ )	$(4.2^{+0.4}_{-0.4})$	$(4.2^{+0.4}_{-0.4})$	$(4.2^{+0.4}_{-0.4})$
$kT_{\text{bb}}$ (eV)	$134^{+2}_{-4}$	$119^{+2}_{-2}$	$90^{+3}_{-3}$
$R_{\text{bb}}$ ( $10^3$ km)	$10.5^{+0.3}_{-0.3}$	$10.5^{+0.3}_{-0.3}$	$18.4^{+0.9}_{-1.0}$
$kT_{\text{edge}}$ (keV)	$(1.07^{+0.03}_{-0.05})$	$(1.07^{+0.03}_{-0.05})$	$(1.07^{+0.03}_{-0.05})$
$\tau_{\text{edge}}$	[0]	$2.1^{+1.3}_{-0.8}$	[0]
$kT_{\text{mekal1}}$ (keV)	$(0.61^{+0.06}_{-0.07})$	$(0.61^{+0.06}_{-0.07})$	$(0.61^{+0.06}_{-0.07})$
$N_{\text{mekal1}}$	$1.9^{+1.2}_{-1.2} \times 10^{-5}$	$2.3^{+0.4}_{-0.4} \times 10^{-5}$	[0]
$kT_{\text{mekal2}}$ (keV)	$(0.99^{+0.16}_{-0.15})$	$(0.99^{+0.16}_{-0.15})$	$(0.99^{+0.16}_{-0.15})$
$N_{\text{mekal2}}$	$4.0^{+1.4}_{-1.2} \times 10^{-5}$	$< 0.30 \times 10^{-5}$	[0]
$kT_0$ (eV)	$(134^{+2}_{-4})$	$(119^{+2}_{-2})$	$(90^{+3}_{-3})$
$kT_e$ (keV)	[4.0]	[4.0]	[4.0]
$\tau_e$ (keV)	(> 2.0)	(> 2.0)	(> 2.0)
$N_{\text{comptt}}$	$7.2^{+7.3}_{-6.6} \times 10^{-6}$	$< 2.6 \times 10^{-6}$	[0]
$\chi^2_\nu$	(1.21 (174.1/144))	(1.21 (174.1/144))	(1.21 (174.1/144))
$f_{0.3-10}$ ( $10^{-13}$ erg cm $^{-2}$ s $^{-1}$ )	$5.9^{+0.2}_{-0.2}$	$2.9^{+0.2}_{-0.2}$	$1.6^{+0.3}_{-0.3}$
$L_{0.3-10}$ ( $10^{39}$ erg s $^{-1}$ )	$4.4^{+0.2}_{-0.2}$	$2.3^{+0.2}_{-0.2}$	$1.5^{+0.3}_{-0.3}$
$L_{\text{bb}}^{\text{bol}}$ ( $10^{39}$ erg s $^{-1}$ )	$4.5^{+0.2}_{-0.3}$	$2.9^{+0.2}_{-0.2}$	$2.9^{+0.3}_{-0.3}$

**Table A3.** Best-fitting spectral parameters for the three intra-observation intervals of ObsID 934, fitted with  $\text{pileup} \times \text{tbabs} \times \text{tbabs} \times \text{edge} \times (\text{mekal} + \text{mekal} + \text{blackbody} + \text{comptt})$ . Parameters listed in square brackets were frozen during the fit; parameters listed in round brackets were free but locked for all three spectra; all other parameters were left free to vary independently. The *mekal* normalization is in units of  $10^{-14}/(4\pi d^2) \int n_e n_H dV$ . Errors indicate the 90% confidence interval for each parameter of interest. This model is statistically and visually indistinguishable from the three-temperature *mekal* model of Table A2.

	2000 Oct 29	2004 Jul 5–11	2004 Dec 22–24	2004 Dec 30	2005 Jan 1	Faint state
Parameter	Value					
$g_0$					[1]	
$\alpha$					$1.00^{+*}_{-0.25}$	
psfrac					[0.85]	
$N_{\text{H,Gal}}$ ( $10^{20}$ cm $^{-2}$ )	[1.5]	[1.5]	[1.5]	[1.5]	[1.5]	[1.5]
$N_{\text{H,int}}$ ( $10^{20}$ cm $^{-2}$ )	$7.5^{+7.0}_{-4.8}$	$9.7^{+4.0}_{-3.7}$	$20.4^{+13.9}_{-11.5}$	$12.2^{+6.1}_{-5.4}$	$13.4^{+3.2}_{-3.4}$	$19.3^{+15.6}_{-13.3}$
$kT_{\text{bb}}$ (eV)	$77^{+11}_{-10}$	$69^{+7}_{-7}$	$39^{+10}_{-*}$	$75^{+6}_{-6}$	$100^{+13}_{-10}$	$53^{+8}_{-11}$
$R_{\text{bb}}$ ( $10^3$ km)	$29.0^{+32.7}_{-14.4}$	$47.0^{+32.6}_{-17.0}$	> 54	$43.5^{+29.3}_{-17.2}$	$22.5^{+10.3}_{-4.7}$	$24.3^{+102.1}_{-10.8}$
$\Gamma$ (keV)						$1.9^{+0.9}_{-0.7}$
$N_{\text{po}}$ ( $10^{-7}$ )						$3.8^{+2.7}_{-1.6}$
$kT_{\text{edge}}$ (keV)		$0.93^{+0.05}_{-0.04}$				
$\tau_{\text{edge}}$		$2.1^{+1.6}_{-0.9}$				
$kT_{\text{mekal1}}$ (keV)		$0.59^{+0.21}_{-0.26}$			$0.70^{+0.17}_{-0.13}$	
$N_{\text{mekal1}}$		$2.9^{+4.6}_{-1.5} \times 10^{-6}$			$3.1^{+1.5}_{-1.5} \times 10^{-5}$	
$kT_{\text{mekal2}}$ (keV)					$1.3^{+0.2}_{-0.2}$	
$N_{\text{mekal2}}$					$4.3^{+1.7}_{-1.6} \times 10^{-5}$	
$\chi^2_{\nu}$	1.04 (12.4/12)	1.17 (42.1/36)		0.87 (22.5/26)	1.02 (63.0/62)	0.98 (9.8/10)
Cash-stat			26.3/44			
$f_{0.3-10}$ ( $10^{-13}$ erg cm $^{-2}$ s $^{-1}$ )	$1.1^{+0.1}_{-0.2}$	$1.1^{+0.1}_{-0.1}$	$\approx 0.1$	$1.3^{+0.1}_{-0.1}$	$3.2^{+0.1}_{-0.1}$	$0.028^{+0.010}_{-0.007}$
$L_{0.3-10}$ ( $10^{39}$ erg s $^{-1}$ )	$1.6^{+1.8}_{-0.8}$	$2.3^{+1.2}_{-0.8}$	$\approx 1.5$	$3.1^{+2.7}_{-1.3}$	$5.5^{+1.3}_{-1.2}$	$0.11^{+0.06}_{-0.04}$
$L_{\text{bb}}^{\text{bol}}$ ( $10^{39}$ erg s $^{-1}$ )	$3.6^{+6.8}_{-2.0}$	$6.6^{+5.9}_{-2.9}$	> 2.1	$7.7^{+8.6}_{-3.8}$	$6.6^{+1.2}_{-1.0}$	$0.6^{+2.7}_{-0.2}$

**Table A4.** Best-fitting spectral parameters for the other six spectra (some of them single observations, some stacked) plotted in Figure 2. For all spectra, we started with a simple  $tbabs \times tbabs \times blackbody$  model; we included a correction for pileup for the 2005 January 1 observation because of its high count rate. We then added an *edge* and/or *mekal* components for a few epochs, if they significantly improved the fit. The *mekal* normalization is in units of  $10^{-14}/(4\pi d^2) \int n_e n_H dV$ . The *powerlaw* normalization is in photons keV $^{-1}$  cm $^{-2}$  s $^{-1}$  at 1 keV. Errors indicate the 90% confidence interval for each parameter of interest.

	2004 Jul 23	2005 Jan 8
Parameter	Value	
$N_{\text{H,Gal}}$ ( $10^{20}$ cm $^{-2}$ )	[1.5]	[1.5]
$N_{\text{H,int}}$ ( $10^{20}$ cm $^{-2}$ )	$9.8^{+15.4}_{-9.8}$	$11.8^{+4.7}_{-4.2}$
$kT_{\text{bb}}$ (eV)	$48^{+20}_{-25}$	$56^{+5}_{-5}$
$R_{\text{bb}}$ ( $10^3$ km)	$64.7^{+*}_{-54.1}$	$101.5^{+82.7}_{-43.1}$
$\chi^2_{\nu}$	0.92 (7.4/8)	0.80 (27.2/34)
$f_{0.3-10}$ ( $10^{-13}$ erg cm $^{-2}$ s $^{-1}$ )	$0.11^{+0.02}_{-0.02}$	$0.8^{+0.1}_{-0.1}$
$L_{0.3-10}$ ( $10^{39}$ erg s $^{-1}$ )	$0.39^{+*}_{-0.32}$	$2.6^{+1.9}_{-1.0}$
$L_{\text{bb}}^{\text{bol}}$ ( $10^{39}$ erg s $^{-1}$ )	$3.5^{+*}_{-3.3}$	$12.8^{+17.9}_{-6.9}$

**Table A5.** Best-fitting spectral parameters for the combined *XMM-Newton*/EPIC spectrum of the 2004 July 23 and 2005 January 8 observations, plotted in Figure 8. Errors indicate the 90% confidence interval for each parameter of interest.